www.sciencemag.org/content/362/6419/1144/suppl/DC1

Supplementary Materials for

Room-temperature cycling of metal fluoride electrodes: Liquid electrolytes for high-energy fluoride ion cells

Victoria K. Davis, Christopher M. Bates, Kaoru Omichi, Brett M. Savoie, Nebojša Momčilović, Qingmin Xu, William J. Wolf, Michael A. Webb, Keith J. Billings, Nam Hawn Chou, Selim Alayoglu, Ryan K. McKenney, Isabelle M. Darolles, Nanditha G. Nair, Adrian Hightower, Daniel Rosenberg, Musahid Ahmed, Christopher J. Brooks, Thomas F. Miller III, Robert H. Grubbs, Simon C. Jones*

*Corresponding author. Email: simon.c.jones@jpl.nasa.gov

Published 7 December 2018, *Science* **362**, 1144 (2018)
DOI: 10.1126/science.aat7070

This PDF file includes:

Other supplementary material for this manuscript includes the following:

Data S1 (zipped folder)

Materials and Methods

Materials

All compounds and solvents were purchased from Sigma-Aldrich, Alfa Aesar, TCI America, Strem, and/or Fisher and used as-received. NMR solvents were purchased from Cambridge Isotope Laboratories, Inc. Anhydrous diethyl ether was obtained via elution through a solvent column drying system (*27*) and degassed with argon prior to use. Solvents used for solvent screening and electrolyte formulations with dry fluoride salts were dried over 4Å molecular sieves in either a dryroom or an argon filled glovebox. H_2O content (ppm) was monitored via Karl Fisher titration until solvents were anhydrous ($H_2O \leq 16$ ppm). Electrode materials used included: bismuth foil (Alfa Aesar, 1mm thick, 99.999%), lead foil (Alfa Aesar, 0.1mm thick, 99.998%), cerium foil (Alfa Aesar, 0.62mm thick, 99.9%), calcium foil (American Elements, 2mm thick, 99.9%), Super P carbon black (SP; MTI Corporation, TIMCAL Graphite & carbon Super P, Conductive carbon black), and poly(vinylidene fluoride) (PVDF; Alfa Aesar).

Materials Synthesis

Fluoride Salt Synthesis (Np_1F, Two Steps). Trimethylneopentylammonium iodide was prepared from the addition of potassium carbonate (94.1 g, 681 mmol, 2.67 eq) to a 1 L Erlenmeyer flask containing a magnetically stirred solution of methyl iodide (51 mL, 819 mmol, 3.21 eq) and neopentylamine (30 mL, 255 mmol, 1.0 eq) in absolute ethanol (400 mL). After magnetic stirring at room temperature for 21 hours, the mixture was suspended in ethanol (1.25 L), filtered, and the solvent was removed in vacuo. The resulting solid was then suspended in dichloromethane (4 L) and filtered. Solvent was again removed in vacuo and the solid recrystallized from isopropanol (450 mL). The resulting crystals contained 1.6 mol% isopropanol via ^{1}H NMR. Removal of this trace solvent was accomplished by dissolving in water (55 mL) and washing with hexane (3 x 50 mL). Drying in vacuo yielded 48.53 g of white solid (74%). ^{1}H-NMR (300 MHz, CD_3CN) δ 3.38 (2 H, s, $N^+C\mathbf{H}_2C(CH_3)_3$), 3.21 (9 H, s, $N^+(C\mathbf{H}_3)_3$), 1.17 (9 H, s, $N^+CH_2C(C\mathbf{H}_3)_3$). ^{13}C-NMR (126 MHz, $CDCl_3$) δ 76.71, 56.03, 33.73, 30.16. HRMS (EI) calcd. for $C_8H_{20}N$ [H^+] 130.16, found m/z: 130.1596.

Trimethylneopentylammonium fluoride was prepared using an adapted procedure from the literature (*19*). Silver oxide (14.559 g, 62.8 mmol, 1.5 eq) was added to a solution of trimethylneopentylammonium iodide (10.772 g, 41. 9 mmol, 1 eq) in deionized water (225 mL) in an aluminum foil covered 500 mL round bottom flask. After stirring for 1 h, ion-exchange of iodide for hydroxide was quantitatively achieved, as evidenced by the lack of precipitate upon aliquot addition to a solution of silver nitrate in concentrated hydrochloric acid. The suspension was filtered and immediately titrated with aqueous hydrofluoric acid (0.5 wt %). HF was added dropwise and the titration stopped at pH 7.96 (calc. endpt = 8.08). Most of the water was removed under reduced pressure at 60 °C. The solution was further dried by azeotrope with bench-grade isopropanol (x3) at 35 °C. To remove trace silver residue, the solution was filtered (25 mm wheel filter, 0.45 μm PTFE membrane). The solution was transferred into a side arm round bottom flask, and the residual water was removed by azeotrope with dry isopropanol (x5) under high vacuum (~50 mTorr) at 100 °C for five days until Np_1F remained as a white powder, whose F^- singlet peak appears downfield from -75 ppm

(versus DF_2^- normalized to -147 ppm) via ^{19}F NMR. ^1H-NMR (400 MHz, CD_3CN) δ 3.34 (2 H, s, $N^+C\mathbf{H}_2C(CH_3)_3$), 3.26 (9 H, s, $N^+(C\mathbf{H}_3)_3$), 1.18 (9 H, s, $N^+CH_2C(C\mathbf{H}_3)_3$). ^{13}C-NMR (100 MHz, CD_3CN) δ 76.35, 54.96, 33.41, 29.65. ^{19}F-NMR (376 MHz, CD_3CN) δ -74.29 (s, $\mathbf{F}^-$), -147.00 (t, $D\mathbf{F}_2^-$). ^1H NMR and ^{19}F NMR spectra are shown in fig. S17.

Fluoride Salt Synthesis (Np_2F, Five Steps). *N*-(2,2-dimethylpropyl)-2,2-dimethylpropanamide was prepared following a report by Anderson and coworkers (*28*). A 100 mL round bottom flask equipped with a stir bar was charged with neopentylamine (10 mL, 85.5 mmol, 1.23 eq.), triethylamine (12 mL, 85.5 mmol, 1.23 eq.), and chloroform (70 mL), and cooled to 0 °C. Pivaloyl chloride (8.6 mL, 69.5 mmol, 1 eq.) was added drop wise and the resulting solution refluxed (70 °C) for 4 hr. Upon cooling to room temperature, the organic layer was rinsed with deionized water (3x), brine (1x), dried over sodium sulfate, and filtered. The solvent was removed in vacuo to yield an orange solid (11.4 g, 96% yield). ^1H-NMR (300 MHz, $CDCl_3$, 20 °C) δ 5.66 (1 H, bs, O=CN**H**), 3.05 (2 H, d, $NC\mathbf{H}_2C(CH_3)_3$), 1.21 (9 H, s, $O{=}CC(C\mathbf{H}_3)_3$), 0.90 (9 H, s, $NCH_2C(C\mathbf{H}_3)_3$). ^{13}C-NMR (126 MHz, $CDCl_3$) δ 178.32, 50.32, 38.93, 32.09, 27.77, 27.26. HRMS (EI) calcd. for $C_{10}H_{21}NO$ [H^+] 172.2882, found m/z: 172.1700.

N-(2,2-dimethylpropyl)-2,2-dimethylpropan-1-amine was prepared using a procedure adapted from the literature (*29*). In a flame-dried, three-neck flask equipped with a stir bar, lithium aluminum hydride (6.919 g, 182 mmol, 1.5 eq) was suspended in a 5:6 (vol) diethyl ether:dibutyl ether mixture (220 mL) and cooled to 0 °C. *N*-(2,2-dimethylpropyl)-2,2-dimethylpropanamide (20.701 g, 121 mmol, 1.0 eq) was added to the flask and stirred for 30 minutes. The solution was then refluxed for 42 h (120 °C). The mixture was cooled to room temperature, quenched with deionized water, and filtered. The filtrate was treated with concentrated hydrochloric acid until acidic, and water (400 mL) was added to fully dissolve the solid. The water layer was washed with diethyl ether (3x 250 mL), treated with concentrated sodium hydroxide solution until basic, and extracted with diethyl ether (3x 100 mL). The organic layer was dried over sodium sulfate, filtered, and the solvent mostly removed at 40 °C (no vacuum; the amine is volatile). The resulting product was isolated as a slightly yellow clear ethereal solution (47.717 g, 36.1 wt%, 91% yield). ^1H-NMR (500 MHz, $CDCl_3$) δ 2.37 (4 H, s, $N(C\mathbf{H}_2C(CH_3)_3)_2$), 0.94 (18 H, s, $N(CH_2C(C\mathbf{H}_3)_3)_2$). ^{13}C-NMR (126 MHz, $CDCl_3$) δ 63.53, 31.96, 27.76. HRMS (EI) calcd. for $C_{10}H_{23}N$ [H^+] 158.18, found m/z: 158.1908.

N-(2,2-dimethylpropyl)-*N*,2,2-trimethylpropan-1-amine was prepared using a procedure adapted from the literature (*28*). The ethereal solution of *N*-(2,2-dimethylpropyl)-2,2-dimethylpropan-1-amine (16.1 g in diethyl ether (36.1 wt%), 112 mmol, 1 eq) was cooled to 0 °C and formic acid (11.2 mL, 297 mmol, 2.65 eq) was added dropwise. Formaldehyde (8.50 mL (aq. 37 wt%), 145 mmol, 1.30 eq) was added and the mixture refluxed at 60 °C for 22 h. Concentrated hydrochloric acid was added until an acidic pH was reached. The solvent was removed in vacuo at 55 °C, yielding a peach-colored solution. Concentrated sodium hydroxide solution was added until a basic pH was reached. The aqueous layer was extracted with diethyl ether (3x 150 mL). The organic layer was dried over sodium sulfate, filtered, and the solvent mostly removed at 50 °C (no vacuum; the amine is volatile). The resulting product was isolated as a slightly yellow clear ethereal solution (27.454 g, 64.1 wt %, 98% yield). Characterization information was found to correlate with literature values (*28*). ^1H-NMR (300 MHz,

$CDCl_3$, 20 °C) δ 2.30 (3 H, s, NC**H**$_3$), 2.19 (4 H, s, N(C**H**$_2$C(CH$_3$)$_3$)$_2$), 0.88 (18 H, s, N(CH$_2$C(C**H**$_3$)$_3$)$_2$). ^{13}C-NMR (126 MHz, $CDCl_3$) δ 74.68, 48.25, 33.51, 28.91. HRMS (EI) calcd. for $C_{11}H_{25}N$ [H^+] 172.2065, found m/z: 172.2072.

Dimethyldineopentylammonium iodide was prepared from a procedure adapted from the literature (*19*). A solution of *N*-(2,2-dimethylpropyl)-*N*,2,2-trimethylpropan-1-amine in Et_2O (64 mass %, 17.07g, 99.6 mmol, 1 eq), methyl iodide (19 mL, 305 mmol, 3.1 eq), and acetonitrile (85 mL) were added to a 500 mL round bottom flask equipped with a stir bar and refluxed for 5 days. The solvent was then removed in vacuo at 45 °C, and the product was recrystallized from isopropanol to yield 23.826 g off-white crystals (76% yield). ^{1}H-NMR (300 MHz, $CDCl_3$) δ 3.67 (4 H, s, N^+(C**H**$_2$C(CH$_3$)$_3$)$_2$), 3.47 (6 H, s, N^+(C**H**$_3$)$_2$), 1.25 (18 H, s, N^+(CH$_2$C(C**H**$_3$)$_3$)$_2$). ^{13}C-NMR (126 MHz, $CDCl_3$) δ 77.50, 54.23, 34.07, 30.59. HRMS (EI) calcd. for $C_{12}H_{28}N$ [H^+] 186.22, found m/z: 186.2222.

Dimethyldineopentylammonium fluoride was prepared from a procedure adapted from the literature (*19*). Silver oxide (24.616 g, 106 mmol, 1.5 eq) was added to a solution of the iodide salt (22.158 g, 70.7 mmol, 1 eq) in deionized water (330 mL) in an aluminum foil covered 500 mL round bottom flask. After stirring for 1 h, ion-exchange of iodide for hydroxide was quantitatively achieved, as evidenced by the lack of precipitate upon aliquot addition to a solution of silver nitrate in concentrated hydrochloric acid. The suspension was filtered and immediately titrated with aqueous hydrofluoric acid (0.5 wt %). HF was added dropwise and the titration stopped at pH 7.96 (calc. endpt = 8.08). Most of the water was removed under reduced pressure at 60 °C. The solution was further dried by azeotrope with bench-grade isopropanol (x3) at 35 °C. To remove trace silver residue, the solution was micron filtered (25 mm wheel filter, 0.45 μm PTFE membrane). The solution was transferred into a side arm round bottom flask, and the residual water was removed by azeotrope with dry isopropanol (x5) under high vacuum (~50 mTorr) at 100 °C for 5 days until a pale yellow powder remained, whose F^- singlet peak appears downfield from -75 ppm (versus DF_2^- normalized to -147 ppm) via ^{19}F NMR. ^{1}H-NMR (300 MHz, CD_3CN, 20 °C) δ 3.48 (4 H, s, N^+(C**H**$_2$C(CH$_3$)$_3$)$_2$), 3.34 (6 H, s, N^+(C**H**$_3$)$_2$), 1.19 (18 H, s, N^+(CH$_2$C(C**H**$_3$)$_3$)$_2$). ^{13}C-NMR (100 MHz, CD_3CN) δ 77.77, 53.77, 34.06, 30.20. ^{19}F-NMR (282 MHz, CD_3CN, 20 °C) δ -72.87 (s, **F**$^-$), -147.00 (t, D**F**$_2^-$). ^{1}H NMR and ^{19}F NMR spectra are shown in fig. S18.

Copper Nanoparticle Synthesis. Hydrazine hydrate (50-60%, 3 mL, 17.66 M) was added to a stirring solution of hexadecyltrimethylammonium bromide (CTAB) (0.68 g, 1.87 mmol) and citric acid monohydrate (0.08 g, 0.38 mmol) in deionized water (75 mL) under argon at 23 °C. The solution was allowed to age for 20 minutes under argon. Ammonium hydroxide (0.5 mL, 14.5 M) was added to a solution of copper (II) nitrate hemipentahydrate (0.465 g, 2 mmol) and CTAB (0.68 g, 1.87 mmol) in deionized water (75 mL). The copper precursor solution was immediately poured into the hydrazine solution and this mixture was stirred under argon for 2 hours. Copper nanoparticles were isolated via centrifuge (12,000 rpm, 5 min). The supernatant was discarded and the copper nanoparticles were washed with ethanol (10 mL) twice. The product identity was confirmed via pXRD (fig. S19A). The copper nanoparticles have ~50 nm diameter, as determined via TEM imaging (fig. S19B).

Cu@LaF_3 Core-Shell Nanoparticle Synthesis. Copper nanoparticles were prepared as described above. Once copper nanoparticles were isolated via centrifuge (12,000 rpm, 5 min), the supernatant discarded, and the copper nanoparticles washed with

water (30 mL) twice, the Cu nanoparticles were re-dispersed in deionized water (150 mL) and stirred under argon. Hydrazine hydrate (50-60%, 3 mL, 17.66 M) was added to the Cu nanoparticles and stirred for 10 minutes. Both a solution of lanthanum nitrate hexahydrate (0.433 g, 1 mmol) in water (15 mL), and a solution of sodium fluoride (0.042 g, 1 mmol) in water (15 mL) were simultaneously injected into the copper nanoparticle solution over a period of 5 minutes via syringe pump (3 mL/min). The mixture was then stirred for an additional 10 minutes under argon. The core-shell material was isolated via centrifuge (12,000 rpm, 5 min.), the supernatant was discarded, and the remaining core-shell nanoparticles were washed with ethanol (10 mL) twice. Peaks corresponding to both LaF_3 and metallic copper were exhibited by pXRD (fig. S20). Core-shell product identity was confirmed via ICP-MS of the powder (Cu:La:F [atomic %] = 77.5:6.8:15.7), EDX micro analysis (Cu:La:F [at%] = 94.7:1.6:3.7), and EDS elemental mapping (Cu:La:F[at%] = 94.7:1.6:3.7). The copper core has a 50 nm diameter with a 5 nm-thick LaF_3 shell, as determined via TEM imaging (Fig. 3A).

Cu-LaF_3 Thin-Film Preparation. 80 nm of copper (Cu sputtering target) was deposited onto a 5x20 mm area, 1 mm thick glassy carbon (GC) substrate via DC sputtering: 100 W; 3 mTorr; 63A/min sputtering rate. The Cu-coated substrate remained in the chamber to cool down. Then, 4.5 nm of lanthanum fluoride (LaF_3 sputtering target) was deposited on top of the copper thin-film via RF sputtering: 100 W; 3 mTorr; 10Å/min sputtering rate. The coated substrate was then cut into 5x5 mm strips for electrochemical testing. Results from electrochemical testing and XPS are shown in Fig. 3H, Fig. 3I, and fig. S16.

Electrode Fabrication. Bismuth foil, lead foil, cerium foil, and calcium foil were cut into thin strips for use in three-electrode cells. Copper nanoparticles or Cu@LaF_3 core-shell nanoparticles were made into a paste with PVDF and/or SP, pressed into stainless steel mesh, and dried under vacuum prior to three-electrode assembly. The Cu-LaF_3 thin-film was made as described above and assembled into a three-electrode cell. Electrochemical testing details are described in the following section.

Electrochemical Testing

Electrolyte Ionic Conductivity Studies. Ionic conductivities for a number of anhydrous Np_1F and Np_2F solutions were investigated by AC impedance spectroscopy using a VersaSTAT potentiostat. Measurements were acquired between 100 mHz and 1 MHz using an air-free glass conductivity cell including a Teflon ring sealing the solution between two parallel Pt electrodes. The Pt electrodes are separated by ~1 cm, and the cell constant was determined before each experiment by measuring the conductivity of an aqueous potassium chloride (0.1M) solution. Thermal control was provided by a Tenney TUJR chamber, with the sample allowed to reach thermal equilibrium before measurement (as determined by observation of no change in the impedance spectrum over time).

Electrolyte Voltage Window Determination. Fluoride electrolyte solutions were investigated by linear sweep voltammetry using a Bio-Logic VMP2 potentiostat to determine their electrochemical/voltage stability window using a 1 mV/s scan rate. A Pt working electrode, Pt auxiliary, and non-aqueous Ag^+/Ag (MeCN) reference electrode, with Ar purge, were employed for these studies. Voltage windows were determined by two methods: (i) the $J_{cut\text{-}off}$ method, using a limiting current of 100 $\mu A/cm^2$ (Fig. 1I and

fig. S5A), and (ii) the linear fit method (*30*), where voltage limits are defined as the intersection between linear fits of the I-V curves before and after the onset for electrolyte decomposition (fig. S5, B to D, summary data in E).

Solid-Electrolyte Interphase Formation. 1*H*,1*H*,2*H*,2*H*-perfluorooctyltriethoxysilane (FOTS; 0.25 M) was added to 0.75 M Np_1F/BTFE electrolyte. This solution mixture was used in a three-electrode set-up with a Ce or Ca working electrode, Pt wire counter electrode, and silver wire quasi-reference electrode (see table S4). FOTS grafting to Ce or Ca anodes was achieved by cyclic voltammetry (CV) and monitored in situ via electrochemical impedance spectroscopy (EIS). CV parameters: the potential was varied between -0.8V and +0.7 V vs Li^+/Li for 5 cycles using a scan rate of 100 mV/s. EIS parameters: AC impedance spectroscopy measurements were acquired between 0.1 Hz and 0.2 MHz. A Bio-Logic VMP2 potentiostat was used to alternate between CV and EIS electrochemical tests. The initial test was CV followed by EIS, followed by CV, etc. Tests alternated from CV to EIS repeatedly until ten total electrochemical tests had been performed on the Ce or Ca anode. Confirmation of SEI formation on the Ce or Ca anode was achieved via ex situ XPS measurements. An example data set collected using a Ca anode is shown, where odd numbered tests correspond to CV data (fig. S8A) and even numbered tests correspond to EIS data (fig. S8B). XPS analysis of the Ca surface with FOTS grafted is also shown as an example (fig. S8C).

Three-Electrode Assembly and Cycling Details. Bismuth, lead, copper, Cu@LaF_3, Cu-LaF_3 thin-film, calcium, or cerium electrodes were employed as the working electrode in a standard three-electrode cell. Platinum wire was used as the counter electrode and a silver wire in 0.01 M AgTOf/MPPy-TFSI was used as the non-aqueous pseudo-reference electrode. Specific details about each battery, electrolyte composition, and cycling parameters used are listed, along with ICP-MS data of the electrolyte solution after cycling (table S4). Electrochemical charge and discharge cycling was carried out using a VersaSTAT MC potentiostat.

Instrumentation

Nuclear magnetic resonance (NMR) spectra were obtained using either a Mercury Plus 300, Varian 400 MR, Inova 500, or Bruker 400 NMR spectrometer. Chemical shifts for protons are reported in parts per million downfield from tetramethylsilane and are referenced to residual protio-solvent in the NMR solvents: $CDCl_3$ (δ 7.26), CD_3CN (δ 1.96). Data are represented as follows: chemical shift, integration, multiplicity (s = singlet, d = doublet, sep = septet, m = multiplet, br = broad), coupling constants in Hertz (Hz), and assignment. Mass spectrometric data were obtained at the Caltech Mass Spectrometry Facility.

Pulsed-field gradient spin-echo (PFG-SE) ^1H and ^{19}F NMR experiments were performed on a Varian 500 MHz spectrometer with auto-x pfg broadband probe interfaced with a workstation equipped with VnmrJ software (v 4.2). In an Ar filled glovebox, a 5 mm NMR tube was charged with 400 μL of a 0.75 M solution of Np_1F (in BTFE or 3:1 BTFE:DME) or Np_2F (in BTFE) and sealed with a rubber septum and secured using Teflon tape. The NMR tube was removed from the glovebox and flame sealed. The sample was then loaded into the spectrometer and DOSY spectra were recorded (unlocked in pure protio-solvent) at the desired temperature (5 – 40 °C,

increments of 5 °C). The temperature of the probe was calibrated using a methanol standard.

Inductively coupled plasma mass spectrometry (ICP-MS) was operated by Laboratory Testing, Inc. using Thermo iCap-Q-Mass Spec. 3 mL of electrolyte was collected after each electrochemical test. Samples were diluted by water up to 10 mL, such that 10-30% electrolyte was included. Before ICP-MS analysis, samples were shaken to thoroughly mix both the organic and water layers.

Powder X-ray diffraction (pXRD) patterns were collected using Bruker D8 ADVANCE instrument with X-ray generator of 40 kV and 40 mA. Post electrochemical testing samples were loaded into a sealed home-made cell with a Be window to avoid air and moisture. Parameters of pXRD scans were in the range of 10 to 90° 2θ with 0.027 2θ step-size and a count time of 12 sec/step. pXRD patterns of Cu@LaF_3 and Cu precursor powders were collected in air.

Transmission electron microscopy (TEM) and high resolution TEM (HR-TEM) images were collected using an FEI Tecnai F20 operating at 200 kV. Energy dispersive spectroscopy (EDS) was performed using an image-corrected FEI Titan3TM G2 60-300 operating at 300 kV, equipped with a Super-X four quadrant detector. The post electrochemical testing samples were dispersed in anhydrous n-hexane (Aldrich) in a glovebox (H_2O < 0.5 ppm). 20 μL of colloidal suspension (1 mg/1 mL) was drop-cast onto a nickel TEM grid with holey carbon substrate. Samples were vacuum dried for two day before being transferred to the TEM in air. For as-synthesized copper nanoparticles and Cu@LaF_3 nanoparticles, the TEM samples were dispersed in ethanol and drop-cast on a nickel grid.

XPS depth profile analyses were performed by Nanolab Technologies using a K-Alpha^{TM}+ X-ray Photoelectron Spectrometer (XPS) System manufactured by Thermo Fisher Scientific, Inc. Samples were not exposed to X-rays until the measurement was started to minimize the chance of degradation. X-rays are monochromatic Al K_α 1486 eV (8.3383 Å). The etch rate of thermally grown SiO_2 was used as a rough measure of etch depth. The argon ion etch crater size was 4 x 2 mm with an X-ray beam size of 0.4 mm. The Ar^+ etching was performed with an etch rate for SiO_2 of 0.8 Å/sec. Depth profiles were obtained with an Ar^+ beam voltage of 0.5 kV, angle of incidence of 30 degrees, and an etch rate for SiO_2 of 0.8 Å/sec.

STEM pictures and EELS spectra were obtained by using a Jeol2100F microscope equipped with a GIF Tridiem Gatan EELS spectrometer. EELS maps were recorded at 120 kV, and EELS point spectra were taken at 200 kV accelerating voltage. Probe size was 1.5 nm for the mapping and 0.7 nm for the point acquisition. Entrance and exit angles of the electron beam were 12 mrad. Energy resolution was 1.0 eV as measured from the full width half maximum of zero loss peak in vacuum. All EELS spectra were obtained between 390 eV and 1000 eV with 0.3 eV energy steps and 1 sec exposures. Elemental analysis was carried out by using the standard Gatan/EELS software assuming power law for pre-edge background, and a Hartree-Slater model for quantification. For the analysis of La $M_{5,4}$ edge spectra, first the pre-edge background was removed, then two sigmoidal functions of the form $1/(1+e^{-x})$, one at each of the M_5 and M_4 edges, of the same amplitude as the edge jump were subtracted from the data. Least-square fittings of the M_5 and M_4 peaks were carried out by constraining amplitude, loss energy and FWHM. Refined amplitudes were used to calculate the M_5/M_4 ratios.

Samples were transferred to a nitrogen glove bag and dispersed in anhydrous n-hexane (Aldrich). 20 μL of colloidal suspension (1 mg/1 mL) drop-cast onto a Ni TEM grid with holey carbon substrate. Samples were vacuum dried 2 days before TEM analysis. Samples were transferred to the TEM holder in air.

Computational Methods and Calculations

LAMMPS was used to perform all molecular dynamics simulations (*31*). All simulations used a one fs integration time step, Velocity-Verlet integration, and periodic boundary conditions. Long-range electrostatics were modelled using the particle-particle-particle-mesh (PPPM) algorithm (*32*) and Lennard-Jones interactions were truncated at 14 Å. All simulations were initialized from diffuse configurations containing at least 1500 atoms, using a cubic grid to place solvent molecules in random orientations without overlaps. The simulations were first relaxed in the NVE ensemble with restrained atomic displacements of 0.1 Å per time step for 30 ps, followed by a 1 ns NPT equilibration where the temperature was linearly increased from 100 K to 298 K to condense the simulations. The simulations were further equilibrated at 298 K for 2 ns in the NPT ensemble, prior to performing ion insertions for the solvation free energy calculations. In the NPT simulations, the Nosé-Hoover thermostat and barostat were employed using the modified form proposed by Martyna, Tobias, and Klein as implemented in LAMMPS (*33*). For the radial distribution functions (RDFs) reported in the main text, individual ions were randomly inserted into the pre-equilibrated solvent simulations, allowed to further equilibrate in the NPT ensemble for 1 ns, then the RDFs were generated from an additional 10 ns of production data. The radial distribution function for F^- (Fig. 1D) was calculated to characterize the strength of its interaction with the α–CX_2 (X = H or F) moiety of the indicated solvent. In the case of BTFE, there is a large probability of F^- interaction about 2Å from the H atom of the α–CH_2 group; for diglyme, the corresponding probability is considerably reduced. BPFE shows a very small probability of F^- interaction with the F-containing backbone over all separations. The protocols for the free-energy simulations are described in detail in a dedicated section below.

Since several of the solvents presented in this study are novel, suitable force-fields were unavailable from the existing literature. Therefore, all solvent force fields in this study were parameterized on the basis of density functional theory (DFT) quantum chemistry calculations, using the B3LYP-D3/def2-TZVP level of theory computed via the Orca software package (*34*). Following a previously described approach (*35*), the solvent force fields were parameterized using the OPLS force-field function form (*36*), except that 1-4 pairwise interactions were excluded in the non-bonded interaction computation. In brief, bond, angle, and dihedral force-field terms were derived from potential energy curves computed for internal degrees of freedom for each molecule in vacuum, optimizing the other degrees of freedom as a function of the mode scan. The resulting energy curves were self-consistently fit to obtain the corresponding force-constant parameters and equilibrium displacement parameters in the force field. All bond, angle, and dihedral modes for the ions were taken from OPLS (*36*). For all solvents and ions, Lennard-Jones parameters were taken from the universal force field (UFF) (*37*) and partial charges were obtained from CHELPG calculations (*38*) performed on the optimized geometries of the respective molecules.

Quantum chemical calculations were used to characterize the partial charge distribution in BTFE and diglyme (fig. S4). BTFE exhibits larger partial positive charges (0.12) on the hydrogen atoms of the α–CH_2 moiety within the F^- solvation structure than diglyme (0.01), as BTFE has two electron-withdrawing groups flanking the α–CH_2 moiety. Figure 1E depicts the innermost solvation shell of F^- in liquid BTFE (as described in the main text). The solvation shell for the Np_2^+ cation in BTFE is more complex, but qualitatively, the β-CF_3 groups on BTFE appear to be the most prevalent in the Np_2^+ solvation structure (fig. S12). Input files for all simulations are supplied and provide full details of the employed force-field parameters and protocols for the simulations (Data File S1).

Thermodynamic integration was used to calculate the ion-specific solvation free energies in each solvent. Scaled Lennard-Jones (U_{LJ}) and Coulomb (U_C) potentials were used to introduce the ion-solvent potential energy terms gradually in to the solvent-only potential energy terms (U_S) with

$$U_{LJ}(\lambda_{LJ}) = U_S + \lambda_{LJ} U_{LJ} \qquad \textbf{eq. S1}$$

where λ_{LJ} is a linear scaling parameter for the solvent-ion Lennard-Jones interactions (U_{LJ}) and

$$U_C(\lambda_C) = U_{LJ}(1) + \lambda_C U_C \qquad \textbf{eq. S2}$$

where λ_C is a linear scaling parameter for the solvent-ion Coulomb interactions. The potential in eq. S1 was implemented using standard λ–dependent soft-core Lennard-Jones potentials, as implemented in LAMMPS with n = 1 and $\alpha_{LJ} = 0.5$. The potential in eq. S2 was implemented by scaling the charges on the ion by λ_C. The total solvation free-energy was obtained by

$$\Delta G_{TI} = \int_0^1 \langle \frac{dU_{LJ}}{d\lambda_{LJ}} \rangle \, d\lambda_{LJ} + \int_0^1 \langle \frac{dU_C}{d\lambda_C} \rangle \, d\lambda_C \qquad \textbf{eq. S3}$$

The brackets in eq. S3 indicate an ensemble average, and the approximation has been made that the PΔV contribution to the free energy change can be safely neglected. The integrals in eq. S3 were evaluated numerically using the trapezoidal rule, with λ_{LJ} and λ_C incremented in steps of 0.2 (eleven steps total, six for the Lennard-Jones phase and six for the electrostatics, less one redundant step connecting the two phases). The system was allowed to equilibrate for 250 ps at each λ-step, then an additional 250 ps of dynamics were used for calculating the necessary derivatives. The derivatives in eq. S3 were calculated by finite-difference. At endpoints, forward or backward finite-difference was used; at all other points the central difference was used with a λ–step of 0.01 to evaluate the derivative. In the case of the polyatomic cations, an additional free energy contribution associated with removing the intramolecular electrostatics must be computed. Free-energy perturbation was used to evaluate this contribution from a ten ns MD trajectory of the individual cations in vacuum. The reported ΔG_{TI} errors were estimated by bootstrap resampling (5 million samples).

The pKa of acetonitrile, propionitrile, and BTFE were calculated according to

$$pK_{a,i} = a\frac{\Delta G_{-H,i}}{RTln(10)} + b \qquad \textbf{eq. S4}$$

where $\Delta G_{-H,i}$ is the free energy of deprotonation for species i, R is the ideal gas constant, T is 298 K, and a and b are calibration constants obtained by a least-squares fit of eq. S4 to experimental pKa values for reference solvents (1,2,3,4,5-pentamethylcyclopenta-1,3-diene, pKa = 26.1; cyclopenta-1,3-diene, pKa = 18.0; dimethyl 2-(trifluoromethyl)propanedioate, pKa = 10.8; dimethyl 2-methylpropanedioate, pKa = 18.0; dimethyl propanedioate, pKa = 15.9; 1,1,1,3,3,3-hexafluoro-2-(trifluoromethyl)propane, pKa = 11.0; methane, pKa = 56.0; and acetonitrile, pKa = 31.3) (*39–41*). $\Delta G_{-H,i}$ was calculated by first geometry optimizing the neutral and deprotonated species in vacuum, followed by additional geometry optimization using the COSMO polarizable continuum model with a dielectric of 46.7 to match the DMSO reference solvent. After optimizing the geometry, a frequency calculation was performed to obtain the zero-point energy correction to the free energy. The difference in zero-point energy corrected single point energies yielded $\Delta G_{-H,i}$ for each species. All quantum chemistry calculations were performed at the B3LYP-D3/ma-def2-TZVP level of theory. Calculation of solvent pKa values for acetonitrile and propionitrile (fig. S3A) correlate well with those reported in the literature (*42*).

Supplementary Text

Solvent Screening with Np_1F and Long-Term Stability of the F^- Ion in Non-Aqueous Solutions

All solvent screening experiments in this study were carried out inside an argon filled glovebox ($H_2O \leq 10$ ppm). Solvents were purchased commercially and dried over 4Å molecular sieves until anhydrous, as measured via Karl Fisher titration. Purity of all such-treated solvents were confirmed via NMR spectroscopy prior to solvent screening. Solvent screening was carried out by dissolving anhydrous Np_1F in the anhydrous solvent until the solution was saturated. Weights (in grams) of 5 mL oven-dried scintillation vials, solvent, and Np_1F were recorded using an analytical balance inside the glovebox, enabling saturation concentrations (M) of Np_1F in the solvent subsequently to be determined. An aliquot of the saturated solution was then pipetted into an oven-dried NMR tube containing 0.5 mL of CD_3CN NMR solvent, sealed, and then brought out of the glovebox for ^1H and ^{19}F NMR spectroscopy. Characterization of the two reactions, (i) between $C\mathbf{H}_3CN$ and F^- to form $\mathbf{H}F_2^-$, and (ii) between $C\mathbf{D}_3CN$ and F^- to form $\mathbf{D}F_2^-$, is well-established in the literature (*43*). All solvents screened were expected to exhibit a triplet peak in the ^{19}F NMR from $\mathbf{D}F_2^-$ (δ = -147.0 ppm; J = 18 Hz). Because $\mathbf{H}F_2^-$ and $\mathbf{D}F_2^-$ do not undergo fast exchange with each other on the NMR timescale (*17*, *43*), spectra that showed a new triplet peak in the ^1H NMR from $\mathbf{H}F_2^-$ (δ = 16 ppm; J = 121 Hz) and/or a doublet peak in the ^{19}F NMR from $\mathbf{H}F_2^-$ (δ = -146.6 ppm; J = 121 Hz) were considered to be indicative of F^- reaction with the solvent being screened.

Initial screening of Np_1F revealed three broad classes of organic solvents (as described in the main text). Examples of class (b) solvents include nitriles such as acetonitrile (ACN), 2–methoxyacetonitrile, 3–methoxypropionitrile (MeOPN), and pyridines such as 2,6–difluoropyridine, whereas, examples of class (c) solvents include propionitrile (PN), 3–fluorobenzonitrile, and 1–methyl–1–propylpyrrolidinium bis(trifluorosulfonyl)imide (MPPy–TFSI).

Upon determining PN and BTFE to be excellent solvents for stable solvation of the F^- ion, two J. Young NMR tubes were prepared containing anhydrous Np_1F/PN and Np_1F/BTFE solutions respectively (both without CD_3CN NMR solvent) and sealed in inert atmosphere. These J. Young tubes were stored on the benchtop at room temperature for over 140 days while monitoring the long-term stability of the F^- ion via ^1H and ^{19}F NMR (fig. S3B). To our surprise, the initial NMR for both Np_1F/PN and Np_1F/BTFE showed minor traces of HF_2^-. The initial F^- present in these samples was normalized to 100%, relative to the trace HF_2^-. Over time, the $\%HF_2^-$ increases, concurrent with a small, but observable decrease in $\%F^-$.

While the reaction between F^- and CH_3CN are known, it was necessary to explore whether F^- is a strong enough base to deprotonate PN or BTFE. Computational methods were used to calculate the pKa of acetonitrile, PN, and BTFE, as described above. The presence of HF_2^- was never observable in these solutions when CD_3CN NMR solvent was used (fig. S3, C and D). Although the reaction of F^- with CD_3CN is well-characterized (*43*), the analogous behavior of PN and BTFE has not been described in the literature. To explore whether the trace HF_2^- observed arises from reactivity with PN or BTFE, a set of control NMR experiments was carried out using deuterated PN (d_5-PN) and CD_3CN (fig. S3E). In the CD_3CN solution, DF_2^- is observed as expected, arising due to deprotonation

of the acidic CD_3 groups by F^- and no HF_2^- is detected. The reaction of F^- with CD_3CN, therefore, must dominate over reaction with any trace protic impurities (due to the vast excess of CD_3CN). For the d_5-PN solution, the opposite behavior is observed: F^- does not react with the d_5-PN solvent to give DF_2^-, but instead reacts with an unidentified protic impurity (present in trace quantities) to form a minor amount of HF_2^-. In light of this, we conclude that F^- is not a strong enough base to abstract deuterium from d_5-PN under these conditions.

Deuterated BTFE is not commercially available, and our own attempts to synthesize d_4-BTFE were unsuccessful. Computational methods were used to calculate the pKa of acetonitrile, PN, and BTFE, as described above. The calculated values for acetonitrile and PN (fig. S3A) are in excellent agreement with the literature (*42*). Comparing the calculated pKa values of acetonitrile, PN, and BTFE, BTFE appears to be significantly less acidic than PN, and should therefore, be even less reactive as a proton donor to F^-. Hence, we conclude that the traces of HF_2^- observed in Np_1F/PN, Np_1F/d_5-PN, and Np_1F/BTFE solutions (in the absence of CD_3CN) arise from small amounts of unknown protic impurities present in the system, and are not derived from deprotonation of the bulk solvent. Overall, the F^- ion is chemically stable for a long period when stored at room-temperature in anhydrous, non-aqueous liquid solution (e.g. PN or BTFE) under inert atmosphere.

Solution Properties of Ionic Motion in Fluoride-Ion Electrolytes

To fully characterize the ionic properties in liquid solution, pulsed–field gradient spin–echo (PFG–SE) ^1H and ^{19}F NMR and AC impedance measurements were carried out for three electrolyte formulations (tables S1 to S3). An Arrhenius plot of self–diffusivity coefficients ($D_{Np^+} + D_{F^-}$) reveals a higher activation energy for the Np_1F/BTFE electrolyte over the Np_2F/BTFE electrolyte (fig. S13A), whereas activation energies for ionic conduction are comparable for both electrolytes (fig. S13B). The transport numbers for Np^+ cations (t_+) and F^- anions (t_-) were calculated using eq. S5 (*44*):

$$t_+ = \frac{D_{Np+}}{(D_{Np+} + D_{F-})} \quad , \quad t_- = \frac{D_{F-}}{(D_{Np+} + D_{F-})} \qquad \textbf{eq. S5}$$

where D_n is the self-diffusion coefficient (in m^2/s) for the indicated ion, as determined via pulsed-field gradient spin-echo (PFG-SE) ^1H and ^{19}F NMR.

The degree of ion dissociation (α) was calculated using eq. S6 (*45*):

$$\alpha = \frac{\sigma_{AC}}{\sigma_{nmr}} \qquad \textbf{eq. S6}$$

where σ_{AC} is the ionic conductivity (in S/m) determined from AC impedance and σ_{nmr} is the ionic conductivity (in S/m) determined from PFG-SE NMR via the Nernst-Einstein equation (eq. S7) (*45*).

$$\sigma_{\mathrm{nmr}} = \frac{Ne^2}{k_B T}\left(D_{F^-} + D_{Np^+}\right) \qquad \textbf{eq. S7}$$

The Nernst-Einstein equation relates ion diffusion coefficients to ionic conductivity where *N* is the number of ions per m^3, *e* is the elementary charge (in C), k_B is the Boltzmann constant, and T is the temperature (in K). When the degree of ion dissociation is very small ($\alpha << 1$), transport numbers for both anion and cation will be approximately 0.5, indicative of a high degree of ion-pairing within the electrolyte. Ion-pairing can be corrected for using the ion-pair correction factor (ξ), which can be determined using eq. S8 (*44*).

$$\xi = 2D_{Np^+}(\alpha - 0.5) + D_{F-} \qquad \textbf{eq. S8}$$

Transport numbers calculated using eq. S5 assume no ion-pairing occurs. Transport numbers that account for ion-pairing can be calculated using the modified equation (eq. S9) (*44*):

$$t_- = \frac{(D_{F^-} - D_{Np^+} + \xi)}{2\xi} \quad , \quad t_+ = \frac{(D_{Np^+} - D_{F^-} + \xi)}{2\xi} \qquad \textbf{eq. S9}$$

The Stokes radius of either the anion (R_F) or cation (R_{Np}) can be calculated with respect to the solvent (eq. S10) (*45*).

$$R_{F^-} = \frac{D_{solvent}}{D_{F^-}} \quad , \quad R_{Np^+} = \frac{D_{solvent}}{D_{Np^+}} \qquad \textbf{eq. S10}$$

The R-values, rounded to the nearest integer, indicate how many solvent molecules on average diffuse together per every one anion (or cation). This provides an approximate picture for the solvation sphere surrounding a given ion. In the Np_1F/BTFE electrolyte, both the Np_1^+ cation and F^- anion share the same NMR-determined Stokes radii (R_{ion}) value of 2 (Fig. 1H), hence, both ions diffuse together with two BTFE solvent molecules as a tight ion pair, represented qualitatively as "BTFE—Np_1^+—F^-—BTFE." In the Np_2F/BTFE electrolyte, Stokes radii for Np_2^+ and F^- are different, ($R_{Np2} = 3$, $R_F = 2$), indicating unique solvation environments despite ion–pairing, and a situation approaching "$(BTFE)_2$—Np_2^+—BTFE—F^-—BTFE." Hence, the increased degree of ion separation and the greater solvation of the Np_2^+ cation are the contributing factors that influence the lower energy barrier for F^- mobility and resulting improved conductivity in Np_2F/BTFE electrolytes. Results from PFG-SE NMR and AC impedance measurements for three fluoride-ion electrolyte formulations are tabulated (tables S1, S2, and S3).

Supplementary Text for Main Text Fig. 1 Caption

(**B**) Inset: In the case of "stable" solvents such as PN and BTFE no HF_2^- peaks are visible alongside the DF_2^- observed, indicating that H/D exchange induced by trace protic solvent impurity does not occur on the NMR timescale (*17*). (**H**) R_{ion} values represent the number of BTFE solvent molecules that diffuse per ionic species (either the Np_1^+ cation, Np_2^+ cation, or their respective F^- counteranions), and provide a qualitative picture of ion solvation spheres in these electrolytes. Rings are drawn around the data points with BTFE structures to illustrate the number of BTFE molecules surrounding and diffusing with each ion, to approximately depict the solvation spheres. (**I**) Linear sweep voltammograms in main text show smoothed data (via polynomial fits to raw data). See fig. S5 for raw data with overlaid fits.

Interfacial Properties of Fluoride-Ion Electrolytes at Metal Electrode Surfaces

To determine whether this liquid F^- electrolyte is electrochemically active toward promoting conversion reactions at a metal electrode surface, we conducted half-cell experiments with a variety of metal electrode materials. BiF_3, PbF_2, and CuF_2 cathodes have high theoretical specific capacities (302 mAh/g, 219 mAh/g, and 528 mAh/g respectively) and have demonstrated limited cycling in high–temperature FIBs (*23*, *46*–*50*) via direct multivalent conversion avoiding any lower oxidation state intermediate phases such as CuF (*26*, *51*). We achieved electrochemical cycling of Bi, Pb, and Cu electrodes in a 3–electrode cell at room temperature in our liquid electrolytes, whereby up to 10 cycles were demonstrated (Fig. 2, B to E). Powder X–ray diffraction (pXRD) showed conversion of Bi to BiF_3 and Pb to β–PbF_2 upon electrochemical fluorination, whereas the Cu electrode appeared unchanged throughout cycling (fig. S6). In all cases, performance was not ideal: after discharge, BiF_3 peaks were still present in the pXRD pattern, indicating that the conversion reaction is not fully reversible under these conditions. Fluorination and defluorination of Pb appeared to be fully reversible, however, ICP–MS revealed 3.9% dissolution of Pb into the liquid electrolyte after ~7 hours of cycling (similar values for Bi were also measured). Likewise, while electrochemical conversion of Cu to CuF_2 has been shown to occur in solid–state devices, high dissolution (4.0 at%) of Cu was found to occur in liquid electrolyte. Hence, although electrochemical oxidation of Cu presumably occurs, Cu^{2+} dissolves faster than the formation of CuF_2 and/or CuF_2 quickly leaches into the electrolyte upon formation.

This liquid F^- electrolyte is also electrochemically active toward promoting conversion reactions at more electropositive metal surfaces. Half-cell cycling experiments with Ce demonstrated successful fluorination upon first charge to form CeF_3 (fig. S7). After first discharge, however, CeF_3 was only partially defluorinated, indicating that the conversion reaction is not completely reversible under these conditions and electrolyte breakdown may be significant. Such electrolyte breakdown is a common phenomenon that occurs in the first few cycles of battery operation, for example in Li-ion batteries leading to the formation of a passive solid electrolyte interphase (SEI) layer on the anode surface (*24*), which can be tailored to block further electrolyte degradation and electron transport while retaining favorable ionic diffusion properties. Hence, we reasoned that an SEI-promoting additive with the necessary chemical properties (i.e., a sacrificially-reduced, surface-reactive perfluoroalkyl ligand) might improve the cycling properties of electropositive metals, and identified 1*H*,1*H*,2*H*,2*H*-

perfluorooctyltriethoxysilane (FOTS) as a suitable material. Pretreatment of Ca or Ce anodes was carried out through cyclic voltammetry sweeps in 0.75 M Np_1F/BTFE electrolyte containing 0.25 M FOTS additive (fig. S8). The desired formation of a CF_n-containing SEI layer on the metal surface was achieved, as monitored in situ through electrochemical impedance spectroscopy (EIS) and confirmed using ex situ XPS analysis (fig. S8). Notably, use of Ce metal pre-treated with an FOTS-derived SEI layer significantly improved the reversibility of the Ce to CeF_3 conversion reaction (Fig. 2, F and G). However, cycling of Ca was not observed under any conditions investigated; this may indicate that conversion of the higher-coordinate CeF_3 tysonite structure is much more kinetically favorable compared to the more-compact fluorite CaF_2 (note, Ca^{2+} and Ce^{3+} have very similar ionic radii). Nevertheless, from an energy density perspective the increased mass of Ce (or other lanthanide metals) when compared to Ca is substantially off-set by the higher density and three-electron activity of the former (574 mAh/g; 3845 mAh/cm^3 *vs*. 1337 mAh/g; 2073 mAh/cm^3 respectively).

Supplementary Text for Electron Energy Loss Spectroscopy Discussion

LaF_3 was found only in the shell region, while CuF_2 was evident in the interfacial region (Fig. 3F, left inset). Metallic Cu^0 was found in the core, and partially or fully fluorinated Cu states were detected at the interfacial region (Fig. 3F, right inset). Averaged elemental compositions extracted from EELS spectra show Cu–only cores, Cu– and F–containing interfaces, and La– and F–containing shells (Fig. 3G). More fluorine was found in the interface region (30 ± 20 % atom) than within the outer shell (14 ± 12 % atom), indicating that LaF_3 does allow for favorable diffusion of F^- through the shell. As anticipated, La was significantly more abundant in the outer shells (9 ± 8 % atom) than at the interface (1.1 ± 1.3 % atom), supporting that the shell is robust and does not interfere with the chemistry occurring at the interface or core. Comparison of 3D–surface plots for the F K, La $M_{5,4}$, and Cu $L_{3,2}$ edges of both fluorinated and defluorinated particles show that the core–shell nanoparticles maintain their sizes, morphology, and compositions before and after electrochemical cycling (fig. S14). It should be noted that electron beam damage prevented detailed EELS analysis of defluorinated nanoparticles. This is likely due to a softening of the nanoparticle from a crystalline–to–amorphous transformation promoted by residual solvent, with soft matter more prone to electron beam damage (fig. S15).

Supplementary Text for Cu-LaF_3 Thin Film Studies

Thin film structures similar to the Cu@LaF_3 core-shell composition were prepared via sputter deposition onto glassy carbon to give 80 nm Cu core strata covered by a 4.5 nm film of LaF_3. Cyclic voltammetry was carried out as described in the main text. Similarly for the Cu@LaF_3 nanoparticle experiments, no Cu or La was detected in the electrolyte after cycling the thin film electrode. Maximum fluorination of the Cu layer was achieved by electrochemical cycling in liquid electrolyte followed by a potential hold (+3.12 V vs Li^+/Li) for one hour to push the system towards complete conversion of Cu to CuF_2 (Fig. 3H and fig. S16A). Pristine and fluorinated thin–films were analyzed via X–ray photoelectron spectroscopy (XPS), with Ar^+ etching as described in the main text. With optimization of the relative LaF_3 shell thickness and Cu core size, improved

capacity utilization in liquid electrolyte should be achievable. Based on the observed diffusion length, Cu@LaF_3 nanoparticles with a 2 nm shell thickness and a 12 nm diameter core might allow for complete conversion of the Cu core to CuF_2 upon first charge, and much higher practical utilization of the material upon cycling. Additionally, the F^- diffusion length could be improved further through the use of a more conductive shell material than LaF_3, for example $PbSnF_4$ (*52*).

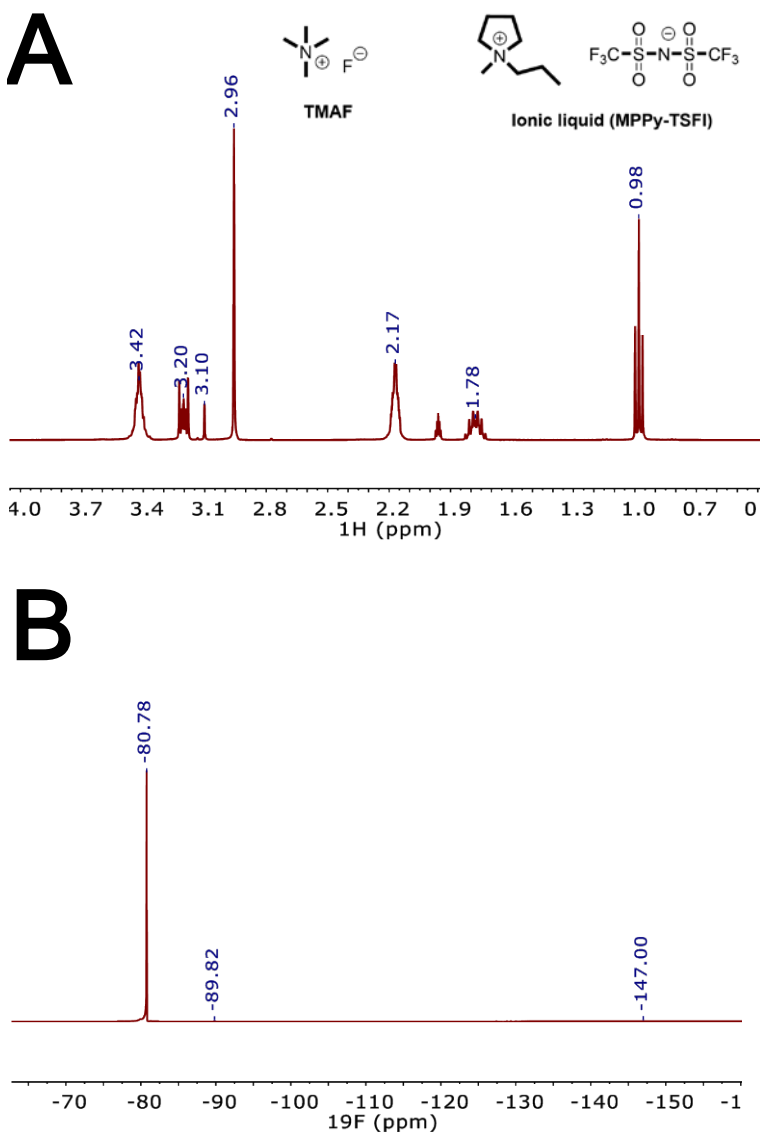

Fig. S1.

Nuclear magnetic resonance spectra of TMAF dissolved in ionic liquid (MPPy-TFSI). (**A**) ^{1}H NMR (400 MHz, CD_3CN) depicts peaks at 3.42 ppm ($MPPy^+$: multiplet, $N^+(C\mathbf{H_2}CH_2)_2$), 3.20 ppm ($MPPy^+$: multiplet, $N^+C\mathbf{H_2}CH_2CH_3$), 3.10 ppm (TMA^+: triplet, $N^+(C\mathbf{H_3})_4$), 2.96 ppm ($MPPy^+$: singlet, $N^+C\mathbf{H_3}$), 2.17 ppm ($MPPy^+$: multiplet, $N^+(CH_2C\mathbf{H_2})_2$), 1.78 ppm ($MPPy^+$: multiplet, $N^+CH_2C\mathbf{H_2}CH_3$), and 0.98 ppm ($MPPy^+$: triplet, $N^+CH_2CH_2C\mathbf{H_3}$). (**B**) ^{19}F-NMR (376 MHz, no NMR solvent) depicts peaks at -80.78 ppm ($TFSI^-$: singlet, $N^-(SO_2C\mathbf{F_3})_2$), -89.82 ppm (singlet, $\mathbf{F}^-$), and -147.00 ppm (triplet, $D\mathbf{F_2}^-$).

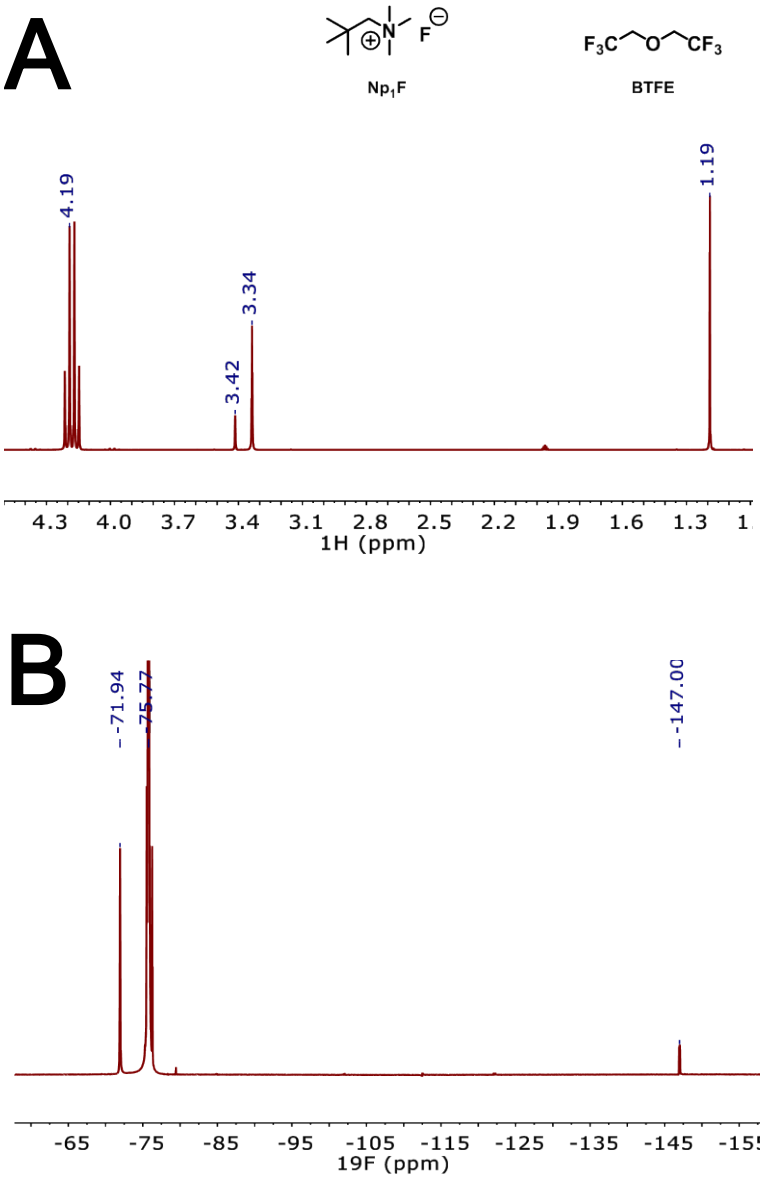

Fig. S2.

Nuclear magnetic resonance spectra of Np_1F dissolved in BTFE. (**A**) ^{1}H NMR (400 MHz, CD_3CN) depicts peaks at 4.19 ppm (BTFE: quartet, $O(C\mathbf{H_2}CF_3)_2$), 3.42 ppm (Np_1^+: singlet, $N^+C\mathbf{H_2}C(CH_3)_3$), 3.34 ppm ($Np_1^+$: singlet, $N^+(C\mathbf{H_3})_3$), and 1.19 ppm (Np_1^+: singlet, $N^+CH_2C(C\mathbf{H_3})_3$). (**B**) ^{19}F-NMR (376 MHz, CD_3CN) depicts peaks at -71.94 ppm (singlet, $\mathbf{F}^-$), -75.77 ppm (BTFE: triplet, $O(CH_2C\mathbf{F_3})_2$), and -147.00 ppm (triplet, $D\mathbf{F_2}^-$).

A

Solvent	Calculated pKa	Literature pKa
Acetonitrile	31	31.3
Propionitrile	33	32.5
BTFE	35	N/A

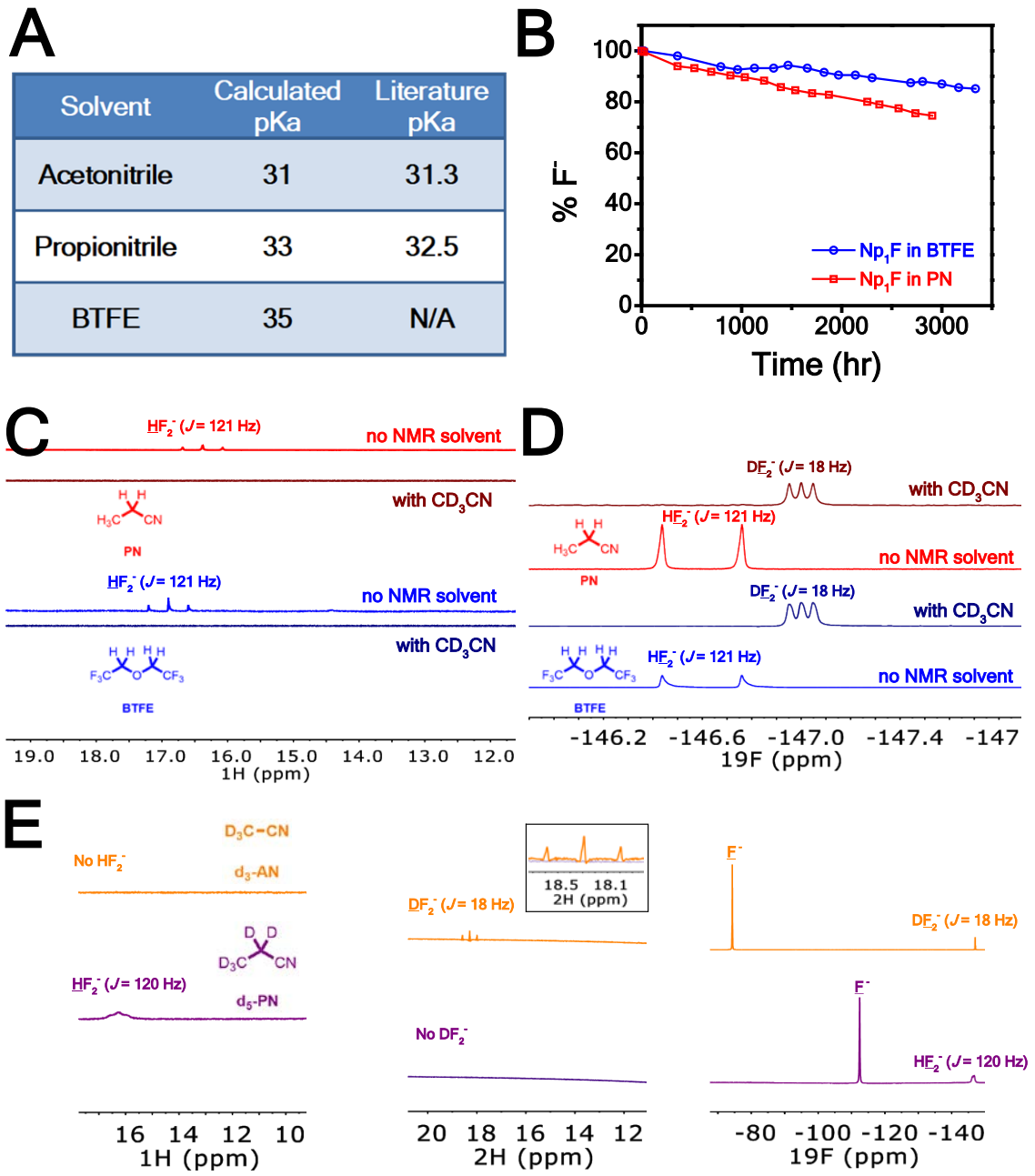

Fig. S3.

Long-term stability of fluoride-ion liquid electrolytes. (**A**) Table of solvent pKa values calculated in this study (see Supplemental Text) and reported in the literature (*42*). **(B)** Long-term monitoring of $\%F^-$ in Np_1F/BTFE (blue circles) and Np_1F/PN (red squares) solutions as determined by ^{19}F NMR (no deuterated NMR solvents were used). Comparison of **(C)** ^1H NMR and **(D)** ^{19}F NMR spectra for Np_1F/PN (red) and Np_1F/BTFE (blue) when CD_3CN NMR solvent is used and when no deuterated NMR solvent is used. **(E)** Control experiments showing ^1H, ^2H, and ^{19}F NMR spectra for Np_1F dissolved in either deuterated acetonitrile (d_3-AN, orange) or deuterated propionitrile (d_5-PN, purple).

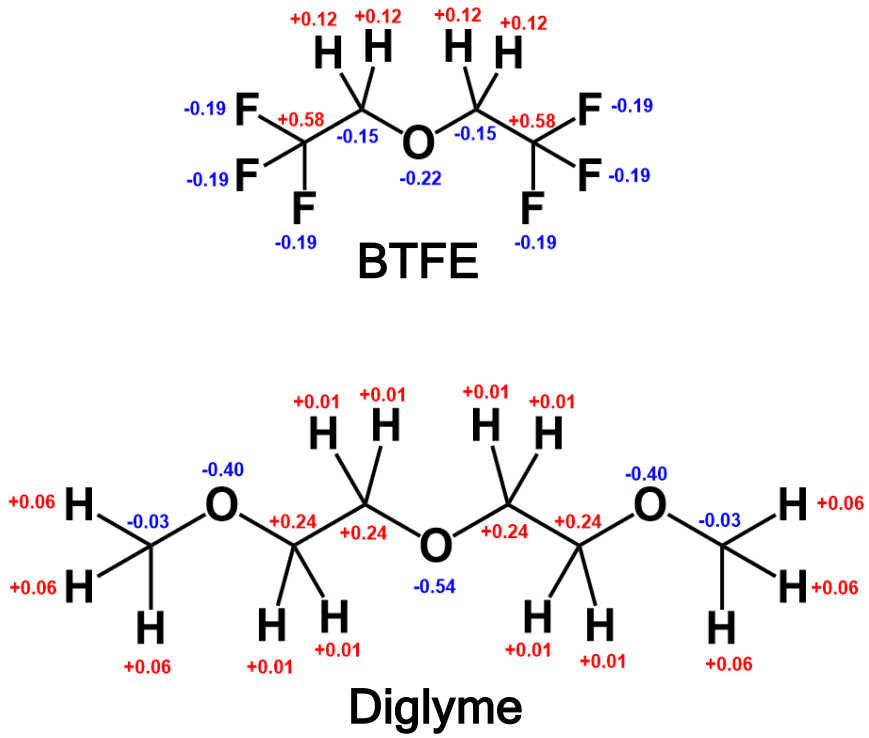

Fig. S4.
Partial charge distribution in the chemical structures of BTFE and diglyme solvents as determined via CHELPG calculations on the B3LYP-D3/def2-TZVP electron densities.

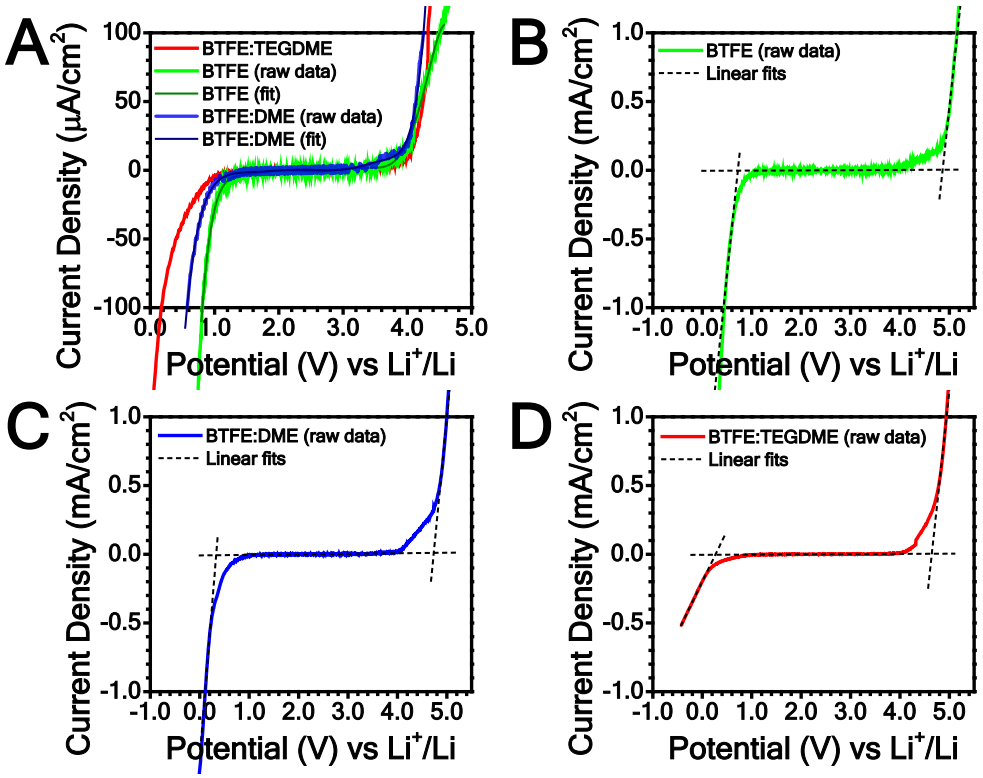

E

	$J_{cut\text{-}off}$ = 100 μA/cm²			Linear Fit Method		
Electrolyte	$V_{limit,\,c}$ (vs Li^+/Li)	$V_{limit,\,a}$ (vs Li^+/Li)	V_{window} (vs Li^+/Li)	$V_{limit,\,c}$ (vs Li^+/Li)	$V_{limit,\,a}$ (vs Li^+/Li)	V_{window} (vs Li^+/Li)
0.75 M Np_1F/ BTFE	0.81	4.50	3.69	0.72	4.86	4.14
0.75 M Np_1F/ BTFE:DME	0.57	4.25	3.68	0.33	4.73	4.40
0.75 M Np_1F/ BTFE:TEGDME	0.17	4.32	4.15	0.26	4.64	4.38

Fig. S5.

Linear sweep voltammetry results for 0.75 M Np_1F in BTFE (green), BTFE:DME (blue), and BTFE:TEGDME (red). (**A**) Raw data for each electrolyte formulation, with simulated fits overlaid on BTFE (dark green) and BTFE:DME (dark blue). Linear regression analysis (dashed lines) of the linear portions of the raw LSV data for (**B**) BTFE, (**C**) BTFE:DME, and (**D**) BTFE:TEGDME electrolytes. (**E**) Table of cathodic voltage limits, anodic voltage limits, and voltage windows determined for each electrolyte formulation using the $J_{cut\text{-}off}$ method or the linear fit method.

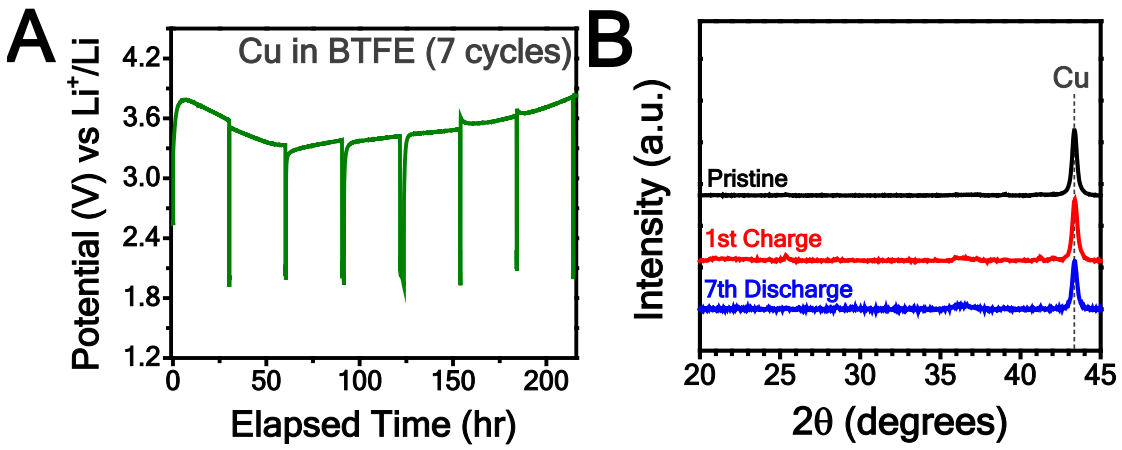

Fig. S6.

Room–temperature performance of copper nanoparticle cathode reversibly cycled in non–aqueous, F^-–conducting liquid electrolytes. (**A**) Voltage profile a Cu cathode collected during electrochemical cycling in a 3–electrode cell. 3–electrode cells were assembled with metal cathode (working electrode), Pt wire (counter electrode), and Ag rod in AgOTf/MPPy–TFSI (reference electrode) in the indicated electrolyte, where IL= 0.1 M TMAF in MPPy–TFSI and BTFE= 0.1 M Np_1F in BTFE. Reference electrode potentials versus Ag^+/Ag were converted to potentials versus Li^+/Li by adding an experimentally–determined reference potential (4.12 V). (**B**) Powder X–ray diffraction (pXRD) patterns obtained for Cu cathodes in pristine condition (black), after first charge or fluorination (red), and after final discharge or defluorination (blue). CuF_2 is not observed (presumably due to Cu^{2+} dissolving into solution).

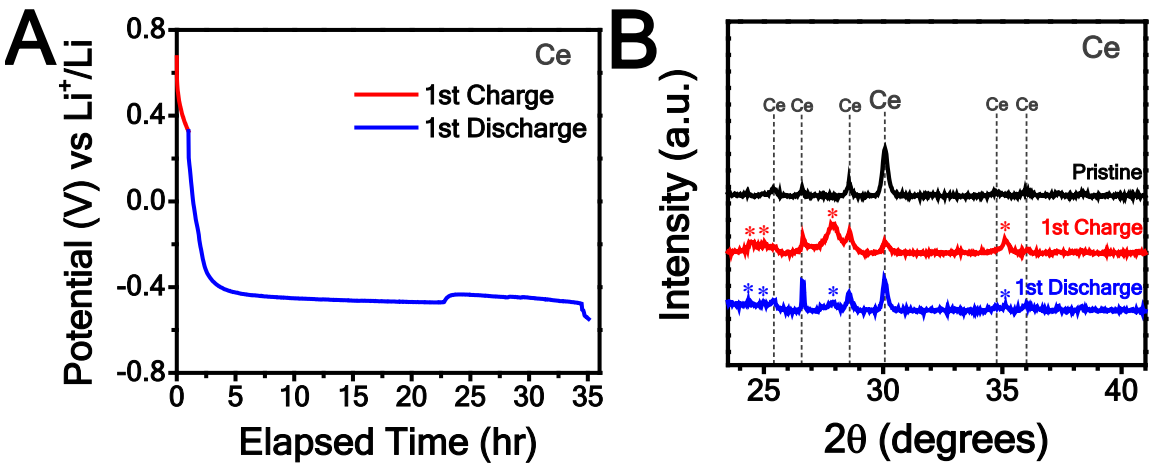

Fig. S7.

Room–temperature conversion reactions on Ce anode material surfaces cycled in non–aqueous, F^-–conducting liquid electrolytes. (**A**) Voltage profile of a Ce anode collected during electrochemical charge and discharge in a 3–electrode cell. (**B**) pXRD patterns obtained for Ce anode in pristine condition (black), after first charge or fluorination (red), and after first discharge or defluorination (blue). Asterisks indicate new peaks corresponding to CeF_3.

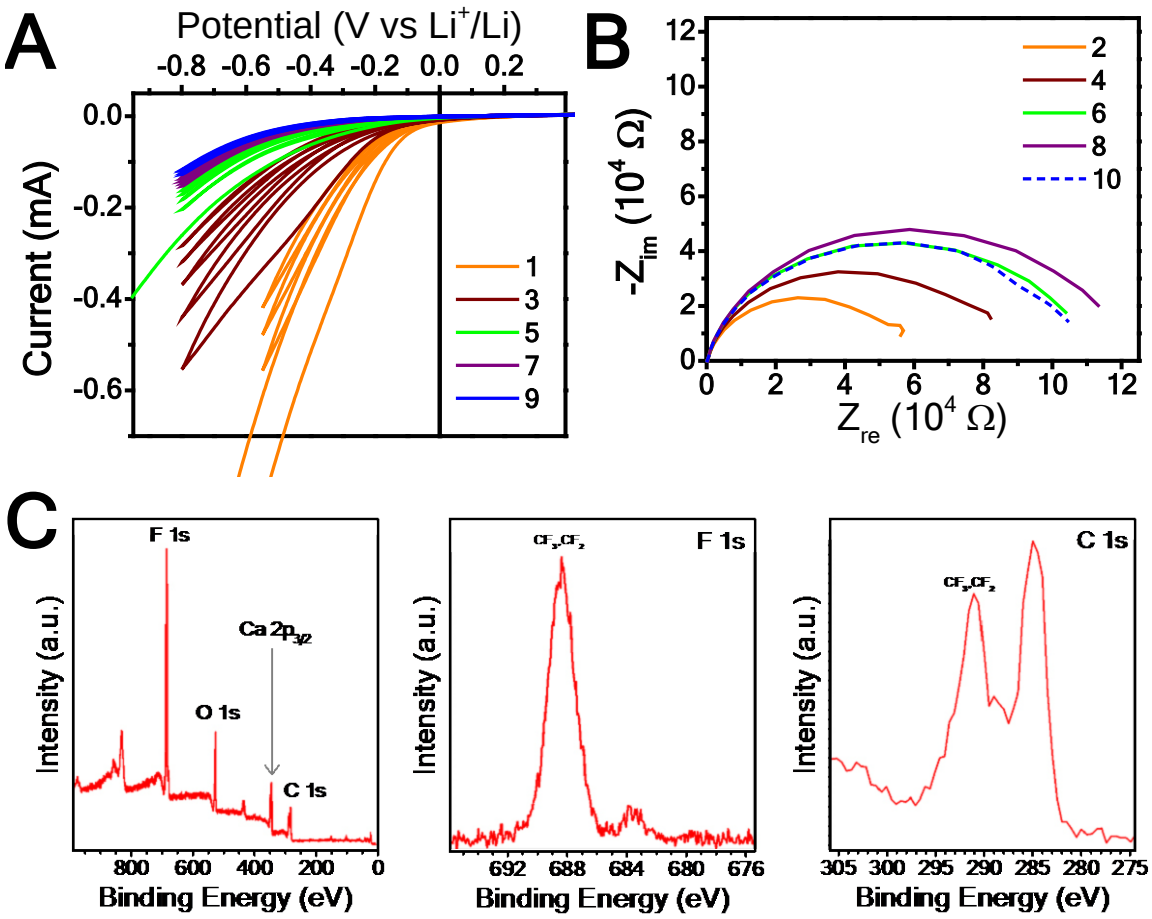

Fig. S8.

Solid-electrolyte interphase formation and characterization of anode materials. Electrochemical grafting of FOTS additive (0.25 M) to the Ce or Ca anode surface was achieved following a standard procedure where electrochemical tests alternated between (**A**) cyclic voltammetry and (**B**) electrochemical impedance spectroscopy studies. Formation of an SEI layer on the Ce or Ca surface was confirmed by (**C**) XPS analysis of the anode after electrochemical grafting experiments. Data shown in (A), (B), and (C) were collected for SEI formation on a Ca anode.

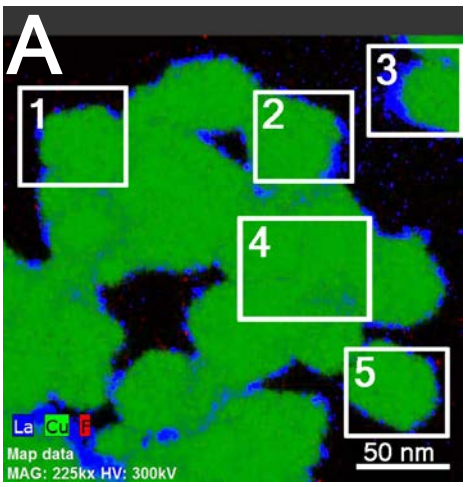

B

EDS Region	Cu (%)	La (%)	F (%)	La : F
1	94.92	1.14	3.94	1 : 3
2	94.82	1.61	3.57	1 : 2
3	91.66	3.27	5.07	1 : 2
4	96.33	0.92	2.75	1 : 3
5	95.53	1.21	3.26	1 : 3
		Average		1 : 3

Fig. S9.

Energy-dispersive X-ray spectrometry (EDS) of pristine Cu@LaF_3 core-shell nanoparticles. (**A**) EDS image of pristine Cu@LaF_3 nanoparticles shows elemental mapping of Cu (green) La (blue), and F (red). (**B**) Table of atomic percentages from EDS regions labeled in (A). Ratios of La to F from all five regions are calculated, averaged, and enumerated in the table.

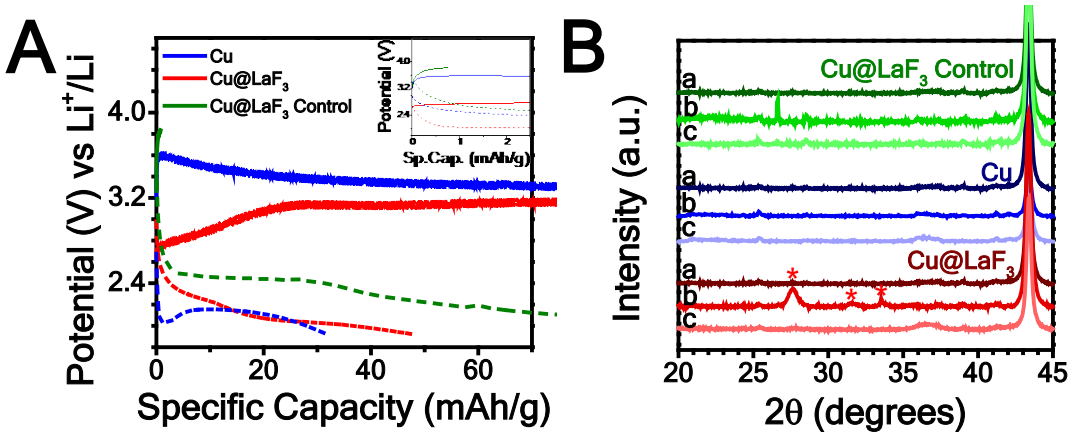

C

Cathode	ICP-MS (µg)	% Dissolution
Cu in 1 M Np_1F/BTFE	180 [Cu]	4.0 [Cu]
$Cu@LaF_3$ in 1 M Np_1F/BTFE	<10 [Cu] <10 [La] (under limit of detection)	<0.2 [Cu] <0.2 [La]
$Cu@LaF_3$ in 0.1 M TBA-TFSI/BTFE	<10 [Cu] <10 [La] (under limit of detection)	<0.1 [Cu] <0.1 [La]

Fig. S10.

Electrochemical cycling, pXRD, and ICP-MS results for copper cathodes in BTFE electrolytes. (**A**) Comparison of the first charge (solid line) and first discharge (dashed line) cycle for Cu in 1 M Np_1F/BTFE (blue), $Cu@LaF_3$ in 1 M Np_1F/BTFE (red), and $Cu@LaF_3$ in 0.1 M tetrabutylammonium bis(trifluoromethane)sulfonimide (TBA-TFSI)/BTFE (green). $Cu@LaF_3$ in 0.1 M TBA-TFSI/BTFE serves as a control experiment where the core-shell cathode was cycled in a battery without a fluoride-ion electrolyte. Inset: expanded region of the plot to visualize better the charge curve for the control experiment. The control cell gained no capacity during first charge; thus, its first discharge curve corresponds to solvent decomposition. (**B**) pXRD spectra of the cathodes (a) in pristine condition, (b) after first charge, and (c) after first discharge. (**C**) Table of ICP-MS data collected from the liquid electrolytes after cycling each cathode.

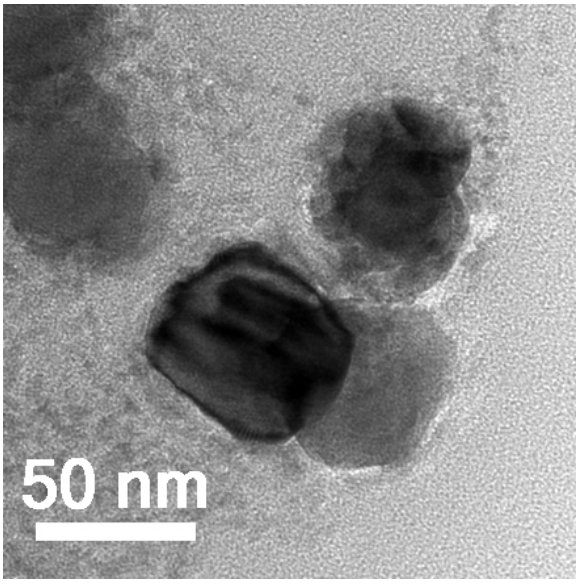

Fig. S11.

TEM image of Cu@LaF_3 nanoparticles, after first charge, where distinct void space (or interface) can be seen between the shell and the core, resembling a yolk-shell structure.

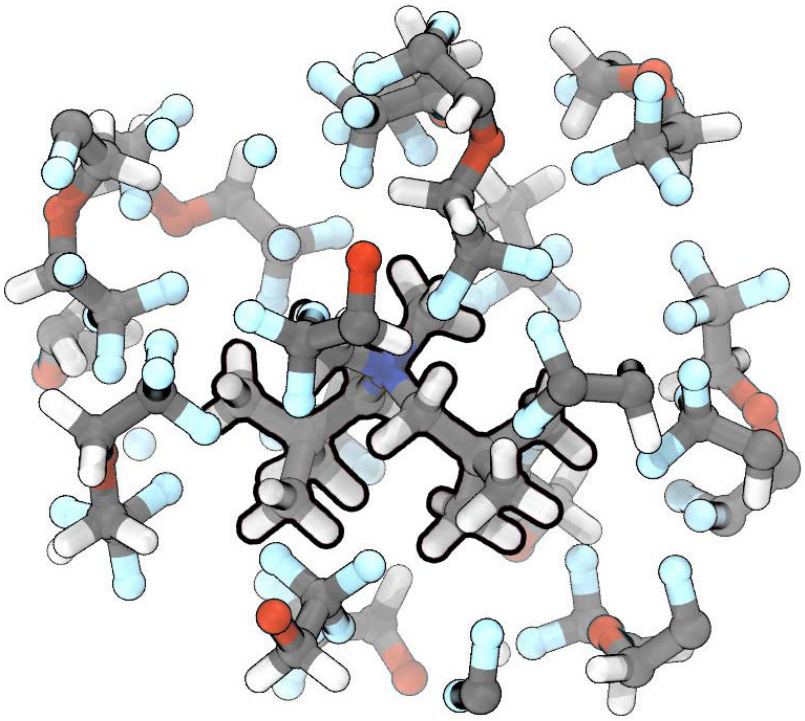

Fig. S12.

Molecular dynamics simulation of the Np_2^+ cation (thick black outline) in BTFE. The atoms of the Np_2^+ cation are approximately 10 Å from the atoms of BTFE in the solvation sphere. Qualitatively, the CF_3 groups on BTFE appear to be most prevalent in the Np_2^+ solvation structure.

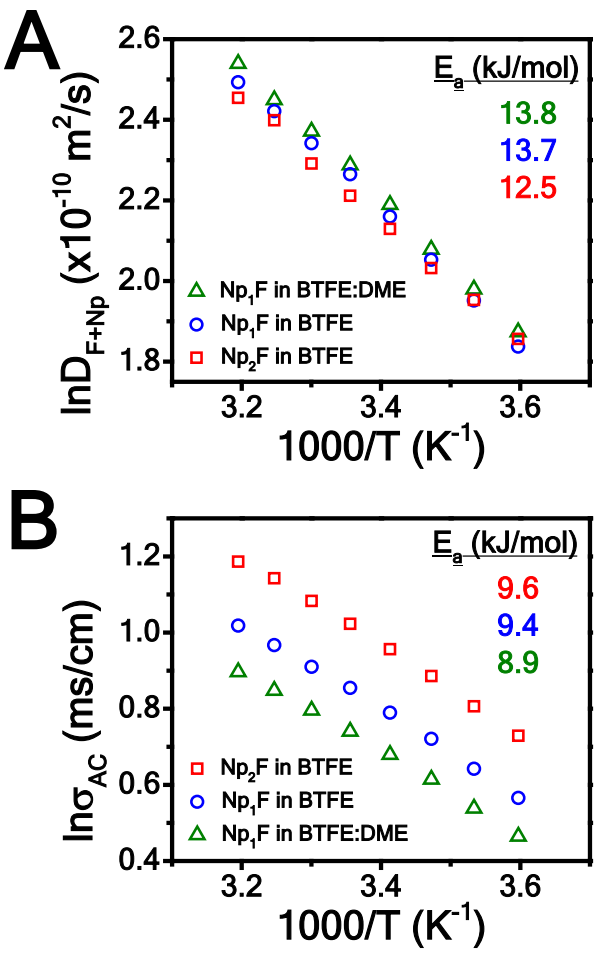

Fig. S13.

Arrhenius analysis of fluoride-ion liquid electrolytes. Arrhenius plots of the (**A**) ionic diffusion constants ($D_{Np^+} + D_{F^-}$) from PFG-NMR, and (**B**) ionic conductivity from AC impedance at temperatures ranging from 5 to 40 °C (in increments of 5 °C) for each of the three electrolyte compositions explored: 0.75 M Np_1F in BTFE (blue circles), 0.75 M Np_2F in BTFE (red squares), and 0.75 M Np_1F in 3:1 BTFE:DME (green triangles).

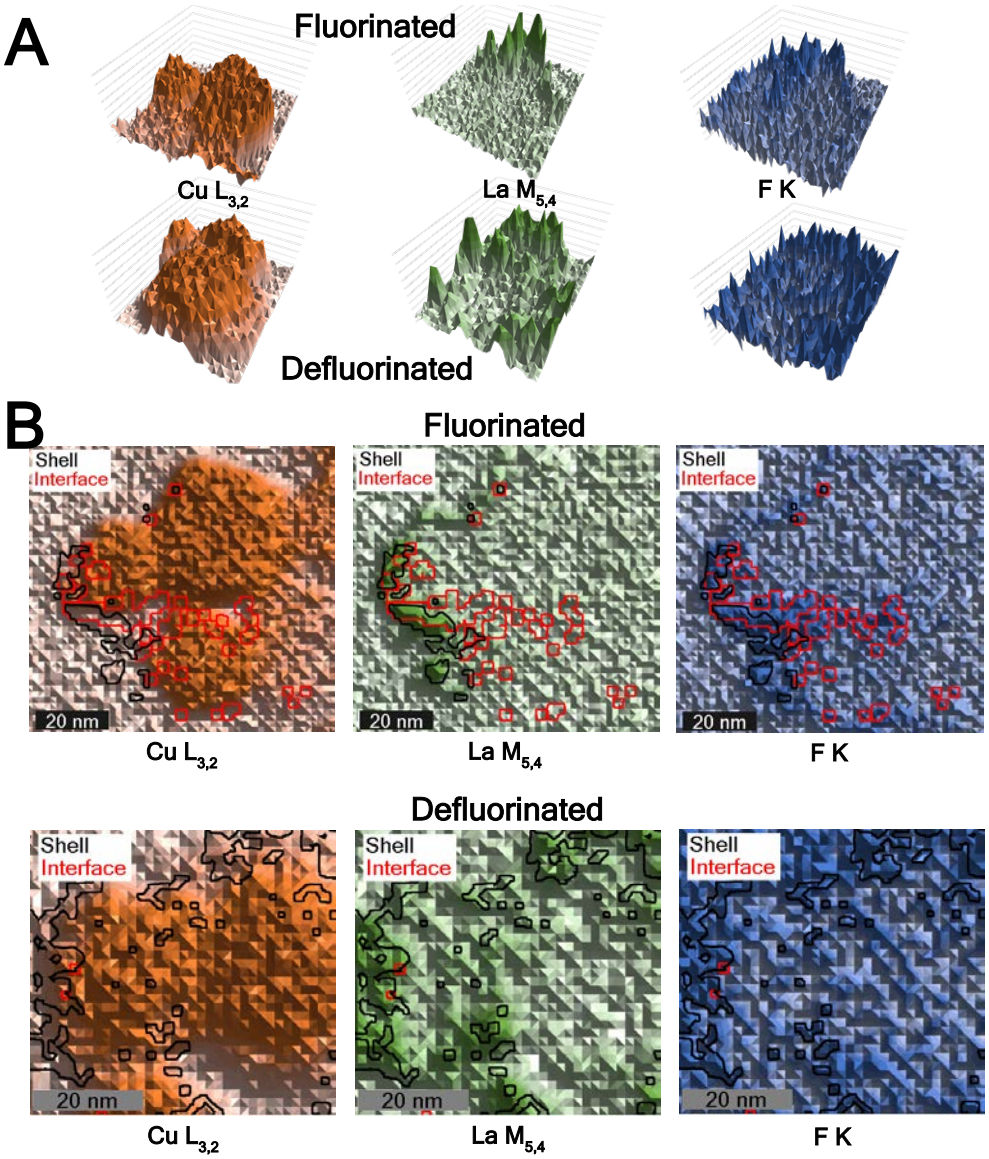

Fig. S14.

Electron energy loss spectroscopy (EELS) maps obtained for fluorinated and defluorinated Cu@LaF$_3$ core-shell nanoparticles. (**A**) 3D surface plots of representative EELS maps obtained at Cu $L_{3,2}$, La $M_{5,4}$, and F K edges for fluorinated (top) and defluorinated (bottom) particles. (**B**) 2D EELS maps obtained at Cu $L_{3,2}$, La $M_{5,4}$, and F K edges for fluorinated (top) and defluorinated (bottom) particles. Shell regions are outlined in black and interface regions are outlined in red.

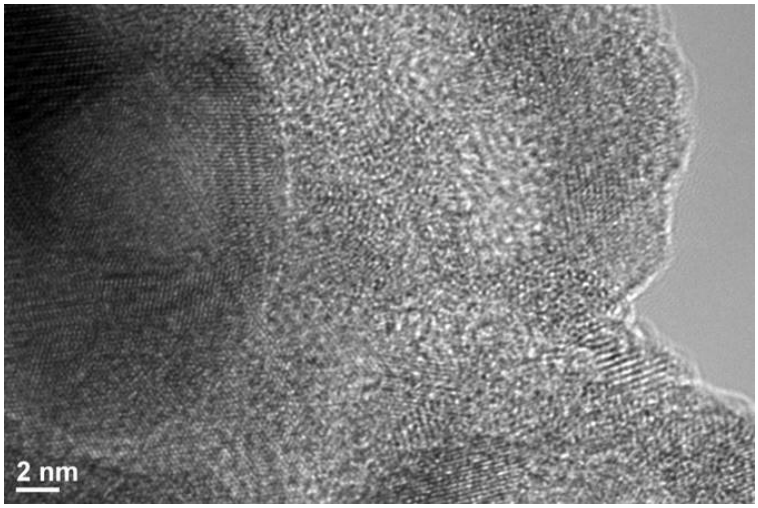

Fig. S15.

TEM image of a Cu@LaF_3 nanoparticle after discharge with visible softening, and spreading out, of the LaF_3 shell.

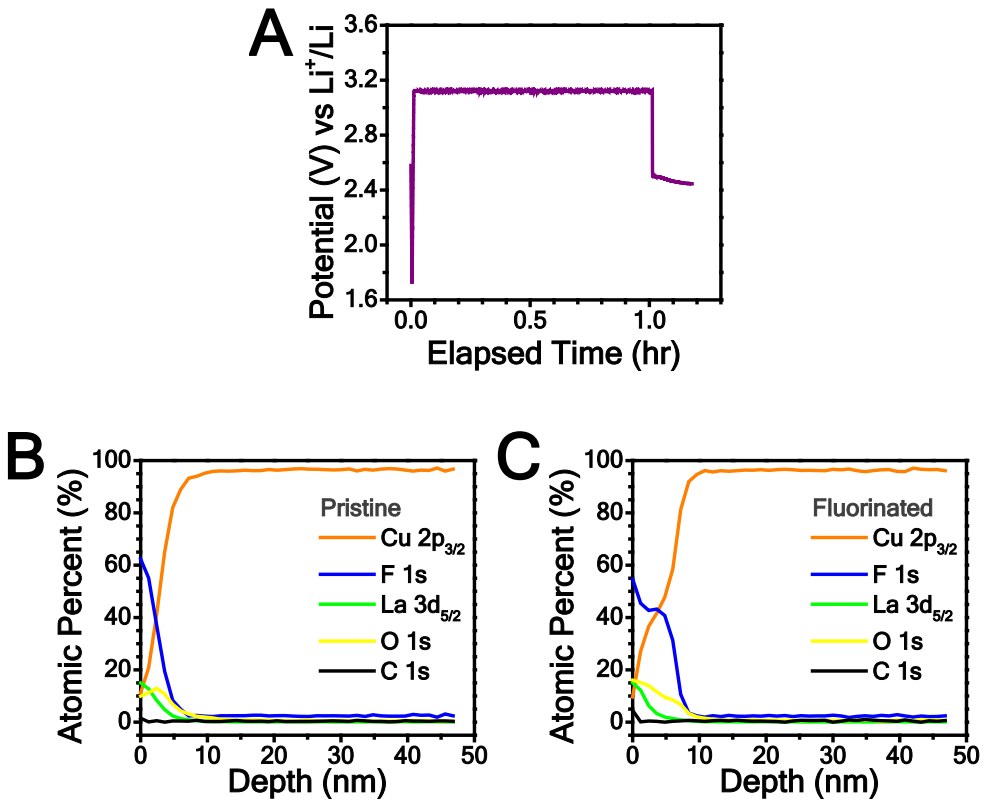

Fig. S16.

Cu-LaF_3 thin-film electrochemistry and XPS depth profiling. (**A**) One-hour potential hold (3.12 V) of Cu-LaF_3 thin-film electrode in 0.1 M TMAF/MPPy-TFSI to ensure electrochemical fluorination. Depth profile of (**B**) pristine and (**C**) fluorinated Cu-LaF_3 thin-film electrode via x-ray photoelectron spectroscopy (XPS) Ar^+ etching rate of 0.8 Å /sec. Etch rate was used to convert etch time (seconds) to sample depth (nanometers).

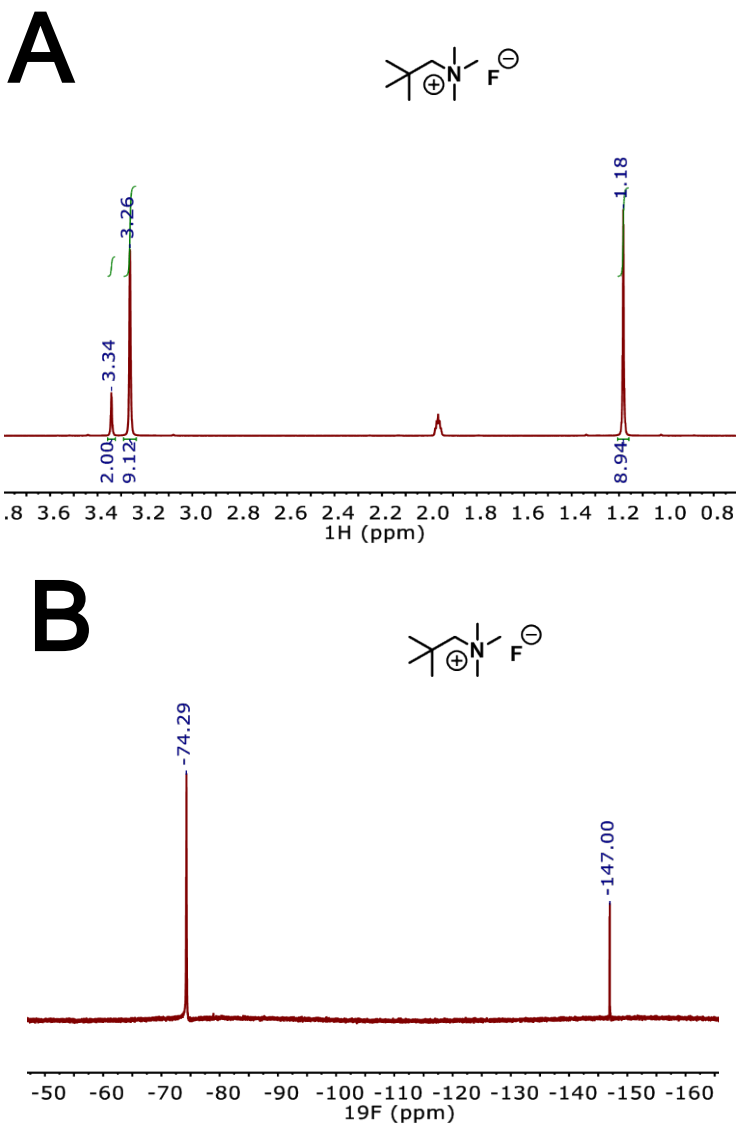

Fig. S17.

Nuclear magnetic resonance spectra of trimethylneopentylammonium fluoride (Np$_1$F). (**A**) ^{1}H NMR (400 MHz, CD_3CN) δ 3.34 (2 H, s, $N^+C\mathbf{H}_2C(CH_3)_3$), 3.26 (9 H, s, $N^+(C\mathbf{H}_3)_3$), 1.18 (9 H, s, $N^+CH_2C(C\mathbf{H}_3)_3$). (**B**) ^{19}F NMR (376 MHz, CD_3CN) δ -74.29 (s, $\mathbf{F}^-$), -147.00 (t, $D\mathbf{F_2}^-$).

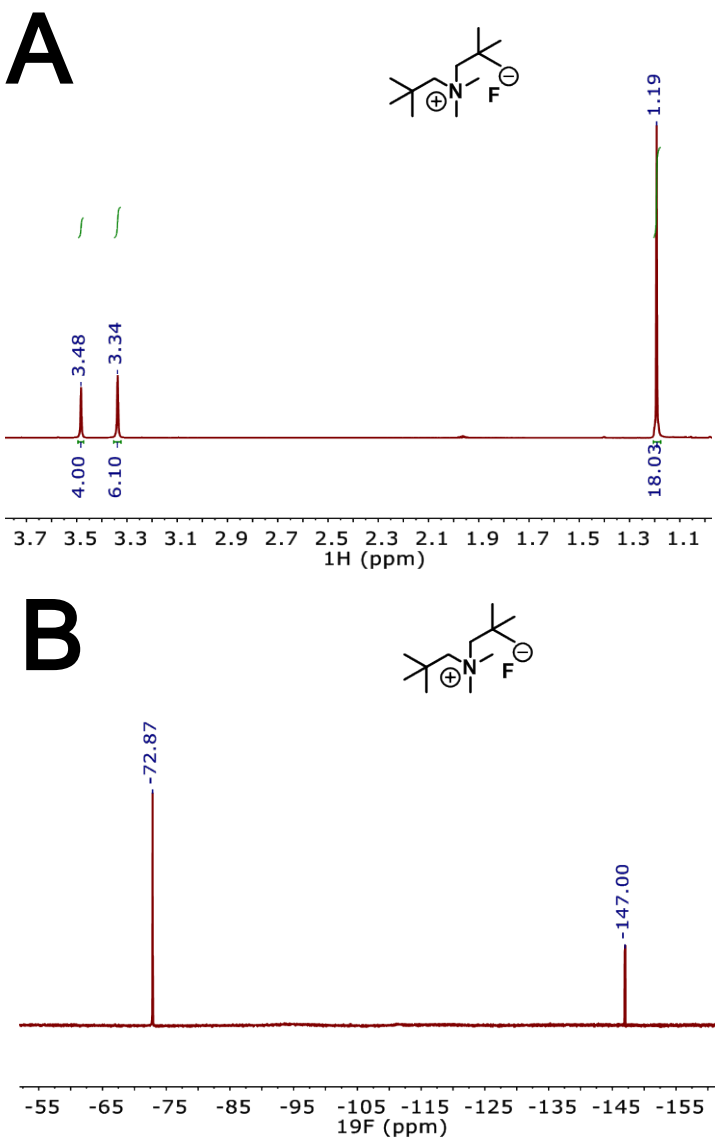

Fig. S18.

Nuclear magnetic resonance spectra of dimethyldineopentylammonium fluoride (Np_2F). (**A**) ^{1}H NMR (300 MHz, CD_3CN, 20 °C) δ 3.48 (4 H, s, $N^+(C\mathbf{H_2}C(CH_3)_3)_2$), 3.34 (6 H, s, $N^+(C\mathbf{H_3})_2$), 1.19 (18 H, s, $N^+(CH_2C(C\mathbf{H_3})_3)_2$). (**B**) ^{19}F NMR (282 MHz, CD_3CN, 20 °C) δ -72.87 (s, $\mathbf{F}^-$), -147.00 (t, $D\mathbf{F_2}^-$).

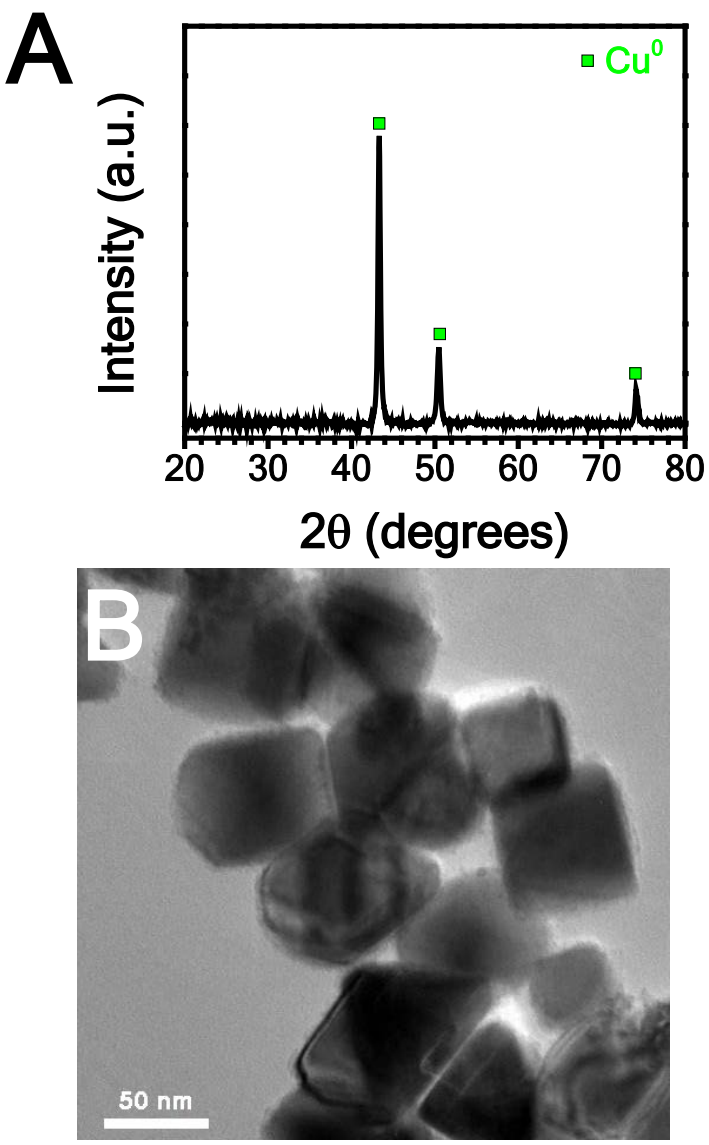

Fig. S19.

pXRD and TEM characterization of pristine powder for the synthesized copper nanoparticles. (**A**) pXRD (Al K_α) spectra of copper nanoparticles. Characteristic peaks for metallic copper (green squares) are depicted. (**B**) TEM image of copper nanoparticles (~50 nm diameter).

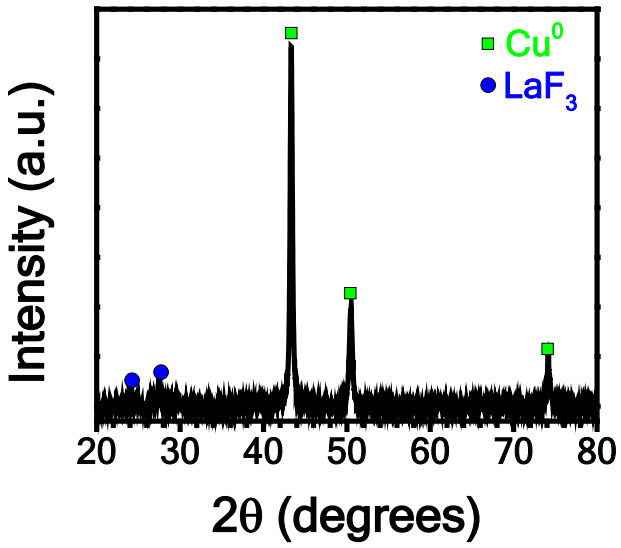

Fig. S20.

pXRD (Al K_α) spectra of pristine powder for the as-synthesized core@shell nanoparticles (Cu@LaF_3). Characteristic peaks for metallic copper (green squares) and lanthanum trifluoride (blue circles) are depicted.

Table S1.

AC impedance ionic conductivity and PFG-SE NMR diffusion measurements for 0.75 M Np_1F in BTFE.

T (°C)	D_F [a] (10^{-10} m²/s)	D_{Np} [a] (10^{-10} m²/s)	D_{BTFE} [b] (10^{-10} m²/s)	t_-	t_+	t_- (ξ corr.)	t_+ (ξ corr.)	σ_{ac} [c] (S/m)	σ_{nmr} (S/m)	α [d]	R_F	R_{Np}
5	3.20 ± 0.01	3.08 ± 0.01	8.07 ± 0.08	0.51	0.49	0.59	0.41	0.1760	1.896 ± 0.009	0.093	3	3
10	3.58 ± 0.01	3.46 ± 0.04	8.8 ± 0.1	0.51	0.49	0.58	0.42	0.1901	2.09 ± 0.02	0.091	2	3
15	3.94 ± 0.06	3.85 ± 0.02	9.8 ± 0.1	0.51	0.49	0.56	0.44	0.2057	2.27 ± 0.03	0.091	2	3
20	4.42 ± 0.02	4.25 ± 0.02	10.8 ± 0.1	0.51	0.49	0.59	0.41	0.2203	2.48 ± 0.02	0.089	2	3
25	4.84 ± 0.03	4.79 ± 0.02	11.1 ± 0.2	0.50	0.50	0.53	0.47	0.2351	2.71 ± 0.02	0.087	2	2
30	5.30 ± 0.04	5.10 ± 0.01	12.8 ± 0.1	0.51	0.49	0.59	0.41	0.2484	2.88 ± 0.02	0.086	2	3
35	5.73 ± 0.01	5.53 ± 0.01	13.8 ± 0.3	0.51	0.49	0.59	0.41	0.2630	3.069 ± 0.008	0.086	2	3
40	6.15 ± 0.05	5.95 ± 0.08	14.5 ± 0.4	0.51	0.49	0.58	0.42	0.2769	3.24 ± 0.05	0.085	2	2

[a]Errors are from VnmrJ program. [b]D_{BTFE} represents the average ± SD of four diffusion coefficients determined for each peak of the quartet corresponding to the methylene protons of BTFE solvent. [c]The error is ± 0.0002 S/m (standard deviation of five measurements). [d]The error is ± 0.001.

Table S2.

AC impedance ionic conductivity and PFG-SE NMR diffusion measurements for 0.75 M Np_2F in BTFE.

T (°C)	D_F [a] (10^{-10} m^2/s)	D_{Np} [a] (10^{-10} m^2/s)	D_{BTFE} [b] (10^{-10} m^2/s)	t_-	t_+	t_- (ξ corr.)	t_+ (ξ corr.)	σ_{ac} [c] (S/m)	σ_{nmr} (S/m)	α [d]	R_F	R_{Np}
5	3.3 ± 0.1	3.14 ± 0.01	7.9 ± 0.2	0.51	0.49	0.58	0.42	0.2073	1.93 ± 0.05	0.107	2	3
10	3.57 ± 0.04	3.48 ± 0.03	8.8 ± 0.1	0.51	0.49	0.55	0.45	0.2239	2.09 ± 0.03	0.107	2	3
15	3.89 ± 0.05	3.74 ± 0.01	9.6 ± 0.2	0.51	0.49	0.58	0.42	0.2425	2.22 ± 0.02	0.109	2	3
20	4.34 ± 0.04	4.07 ± 0.01	10.4 ± 0.2	0.52	0.48	0.62	0.38	0.2602	2.41 ± 0.02	0.108	2	3
25	4.73 ± 0.07	4.40 ± 0.01	11.4 ± 0.2	0.52	0.48	0.63	0.37	0.2781	2.57 ± 0.03	0.108	2	3
30	5.11 ± 0.03	4.78 ± 0.03	12.4 ± 0.2	0.52	0.48	0.62	0.38	0.2954	2.74 ± 0.02	0.108	2	3
35	5.68 ± 0.07	5.33 ± 0.01	13.5 ± 0.4	0.52	0.48	0.62	0.38	0.3136	3.00 ± 0.03	0.105	2	3
40	6.05 ± 0.04	5.59 ± 0.03	15.0 ± 0.2	0.52	0.48	0.64	0.36	0.3275	3.12 ± 0.03	0.105	2	3

[a]Errors are from VnmrJ program. [b]D_{BTFE} represents the average ± SD of four diffusion coefficients determined for each peak of the quartet corresponding to the methylene protons of BTFE solvent. [c]The error is ± 0.0002 S/m (standard deviation of five measurements). [d]The error is ± 0.001.

Table S3.

AC impedance ionic conductivity and PFG-SE NMR diffusion measurements for 0.75 M Np_1F in BTFE:DME (3:1).

T (°C)	D_F [a] (10^{-10} m²/s)	D_{Np} [a] (10^{-10} m²/s)	D_{BTFE} [b] (10^{-10} m²/s)	D_{DME} [a] (10^{-10} m²/s)	t_-	t_+	t_- (ξ corr.)	t_+ (ξ corr.)	σ_{ac} [c] (S/m)	σ_{nmr} (S/m)	α [d]	R_F BTFE | DME	R_{Np} BTFE | DME
5	3.33 ± 0.03	3.18 ± 0.01	8.3 ± 0.2	10.61 ± 0.09	0.51	0.49	0.61	0.39	0.1591	1.97 ± 0.02	0.0810	2 | 1	2 | 1
10	3.68 ± 0.02	3.56 ± 0.02	9.2 ± 0.2	11.84 ± 0.05	0.51	0.49	0.59	0.41	0.1713	2.15 ± 0.02	0.0798	2 | 1	2 | 1
15	4.14 ± 0.03	3.85 ± 0.03	10.1 ± 0.2	13.18 ± 0.09	0.52	0.48	0.66	0.34	0.1848	2.33 ± 0.02	0.0794	2 | 1	2 | 1
20	4.56 ± 0.03	4.37 ± 0.02	11.2 ± 0.2	14.46 ± 0.02	0.51	0.49	0.61	0.39	0.1973	2.56 ± 0.02	0.0771	2 | 1	2 | 1
25	5.03 ± 0.04	4.82 ± 0.03	12.6 ± 0.7	14.59 ± 0.02	0.51	0.49	0.61	0.39	0.2097	2.77 ± 0.03	0.0756	2 | 1	2 | 1
30	5.52 ± 0.02	5.19 ± 0.03	13.3 ± 0.3	17.44 ± 0.09	0.52	0.48	0.65	0.35	0.2216	2.97 ± 0.02	0.0747	2 | 1	2 | 1
35	5.88 ± 0.03	5.70 ± 0.02	14.4 ± 0.3	18.73 ± 0.03	0.51	0.49	0.59	0.41	0.2334	3.16 ± 0.02	0.0740	2 | 1	2 | 1
40	6.47 ± 0.01	6.20 ± 0.02	15.7 ± 0.4	19.86 ± 0.07	0.51	0.49	0.62	0.38	0.2451	3.40 ± 0.01	0.0721	2 | 1	2 | 1

[a]Errors are from VnmrJ program. [b]D_{BTFE} represents the average ± SD of four diffusion coefficients determined for each peak of the quartet corresponding to the methylene protons of BTFE solvent. [c]The error is ± 0.0002 S/m (standard deviation of five measurements). [d]The error is ± 0.0006.

Table S4.

Compositional information, electrochemical testing parameters, and ICP-MS results of fluoride-ion electrochemical cells described.

Battery Composition	Test Parameters	ICP-MS [indicated element] (μg)
WE: Bi foil (146.4 mg; 3x5 mm) **CE: Pt wire** **RE: 0.01 M AgOTf/MPPy-TFSI** **Electrolyte: 0.1 M TMAF/MPPy-TFSI**	Charge to: 2.82 V vs Li^+/Li 200 μA (1 hour cut off) Discharge to: 1.72 V vs Li^+/Li 50 μA (voltage cut off)	463 [Bi]
WE: Pb foil (11.2 mg; 2x5 mm) **CE: Pt wire** **RE: 0.01 M AgOTf/MPPy-TFSI** **Electrolyte: 0.1 M Np_1F/BTFE**	Charge to: 2.42 V vs Li^+/Li 300 μA (1 hour cut off) Discharge to: 1.72 V vs Li^+/Li 25 μA (voltage cut off)	441 [Pb]
WE: Cu:PVDF (90:10; 4.55 mg) **CE: Pt wire** **RE: 0.01 M AgOTf/MPPy-TFSI** **Electrolyte: 1 M Np_1F/BTFE**	Charge to: 3.82 V vs Li^+/Li 10 μA (60 hours cut off; never reached 3.82 V) Discharge to: 1.92 V vs Li^+/Li (voltage cut off)	180 [Cu]
WE: Cu@LaF_3:PVDF:SP (8:1:1; 5.62 mg) **CE: Pt wire** **RE: 0.01 M AgOTf/MPPy-TFSI** **Electrolyte: 1 M Np_1F/BTFE**	Charge to: 3.82 V vs Li^+/Li 10 μA (60 hours cut off; never reached 3.82 V) Discharge to: 1.92 V vs Li^+/Li 10 μA (voltage cut off) Note: only 7 cycles were obtained due to electrolyte evaporation during cycling	<10 [Cu] <10 [La] (under limit of detection)
WE: Cu@LaF_3:PVDF:SP (8:1:1; 6.74 mg) **CE: Pt wire** **RE: 0.01 M AgOTf/MPPy-TFSI** **Electrolyte: 0.1 M TBA-TFSI/BTFE**	Charge to: 3.835 V vs Li^+/Li 10 μA (100 hours cut off; never reached 3.835 V) Discharge to: 1.92 V vs Li^+/Li 10 μA (voltage cut off)	<10 [Cu] <10 [La] (under limit of detection)
WE: Cu-LaF_3 thin-film on GC **(4.5 nm LaF_3:80 nm Cu:1 mm GC)** **CE: Pt wire** **RE: 0.01 M AgOTf/MPPy-TFSI** **Electrolyte: 0.1 M Np_1F/PN**	CV: 10 cycles 1.72 V to 3.32 V vs Li^+/Li 50 mV/s scan rate Potential hold: 3.12 V vs Li^+/Li (1 hour)	<10 [Cu] <10 [La] (under limit of detection)
WE: Ce foil (62.96 mg; 5x3 mm) **CE: Pt wire** **RE: 0.01 M AgOTf/MPPy-TFSI** **Electrolyte: 0.75 M Np_1F/BTFE**	Charge to: 3.785 V vs Li^+/Li 30 μA (1 hour cut off) Discharge to: -0.715 V vs Li^+/Li 30 μA (34 hours cut off)	N/A
WE: Ce foil (62.96 mg; 5x3 mm) with SEI layer **CE: Pt wire** **RE: 0.01 M AgOTf/MPPy-TFSI** **Electrolyte: 0.75 M Np_1F/BTFE** **SEI additive: 0.25 M FOTS**	Charge to: 3.785 V vs Li^+/Li 30 μA (1 hour cut off; never reached 3.785 V) Discharge to: -0.715 V vs Li^+/Li 30 μA (41 hours cut off; never reached -0.715 V)	N/A

Data File S1. (separate file)

This directory provides access to example inputs and force-field parameters that are employed in the molecular dynamics simulations. The first level of the directory tree indicates the solvent. Within each solvent directory, there are additional folders that indicate the studied ion. Within each ion-labeled directory, the *.data file is a typical LAMMPS data file, the *in.init is a LAMMPS input file that defines the simulation conditions, the *in.settings file is an auxiliary file that reports force-field parameters, and the *.map file provides information on each of the simulated atoms.

References

1. D. Larcher, J. M. Tarascon, Towards greener and more sustainable batteries for electrical energy storage. *Nat. Chem.* **7**, 19–29 (2015). doi:10.1038/nchem.2085 Medline

2. A. Manthiram, Y. Fu, S. H. Chung, C. Zu, Y. S. Su, Rechargeable lithium-sulfur batteries. *Chem. Rev.* **114**, 11751–11787 (2014). doi:10.1021/cr500062v Medline

3. A. C. Luntz, B. D. McCloskey, Nonaqueous Li-air batteries: A status report. *Chem. Rev.* **114**, 11721–11750 (2014). doi:10.1021/cr500054y Medline

4. R. Mohtadi, F. Mizuno, Magnesium batteries: Current state of the art, issues and future perspectives. *Beilstein J. Nanotechnol.* **5**, 1291–1311 (2014). doi:10.3762/bjnano.5.143 Medline

5. F. Beck, P. Ruetschi, Rechargeable batteries with aqueous electrolytes. *Electrochim. Acta* **45**, 2467–2482 (2000). doi:10.1016/S0013-4686(00)00344-3

6. N. I. Sorokin, B. P. Sobolev, Nonstoichiometric fluorides—Solid electrolytes for electrochemical devices: A review. *Crystallogr. Rep.* **52**, 842–863 (2007). doi:10.1134/S1063774507050148

7. A. A. Potanin, U.S. Patent 7,722,993 B2 (2010).

8. M. Anji Reddy, M. Fichtner, Batteries based on fluoride shuttle. *J. Mater. Chem.* **21**, 17059 (2011). doi:10.1039/c1jm13535j

9. F. Gschwind, Z. Zhao-Karger, M. Fichtner, Fluoride-doped PEG matrix as an electrolyte for anion transportation in a room-temperature fluoride ion battery. *J. Mater. Chem. A Mater. Energy Sustain.* **2**, 1214–1218 (2014). doi:10.1039/C3TA13881J

10. F. Gschwind, J. Bastien, Parametric investigation of room-temperature fluoride-ion batteries: Assessment of electrolytes, Mg-based anodes, and BiF_3-cathodes. *J. Mater. Chem. A* **3**, 5628–5634 (2015). doi:10.1039/C4TA06625A

11. K. Okazaki, Y. Uchimoto, T. Abe, Z. Ogumi, Charge-discharge behavior of bismuth in a liquid electrolyte for rechargeable batteries based on a fluoride shuttle. *ACS Energy Lett.* **2**, 1460–1464 (2017). doi:10.1021/acsenergylett.7b00320

12. H. Konishi, T. Minato, T. Abe, Z. Ogumi, Electrochemical performance of a bismuth fluoride electrode in a reserve-type fluoride shuttle battery. *J. Electrochem. Soc.* **164**, A3702–A3708 (2017). doi:10.1149/2.0931714jes

13. D. A. Wynn, M. M. Roth, B. D. Pollard, The solubility of alkali-metal fluorides in non-aqueous solvents with and without crown ethers, as determined by flame emission spectrometry. *Talanta* **31**, 1036–1040 (1984). doi:10.1016/0039-9140(84)80244-1 Medline

14. H. O. House, E. Feng, N. P. Peet, A comparison of various tetraalkylammonium salts as supporting electrolytes in organic electrochemical reactions. *J. Org. Chem.* **36**, 2371–2375 (1971). doi:10.1021/jo00815a038

15. R. A. Bartsch, Eliminations from 2-butyl halides induced by halide ions in dimethylformamide and dimethyl sulfoxide. *J. Org. Chem.* **35**, 1023–1025 (1970). doi:10.1021/jo00829a035

16. J. S. Martin, F. Y. Fujiwara, High resolution nuclear magnetic resonance spectra of bifluoride ion and its homologues. *Can. J. Chem.* **49**, 3071–3073 (1971). doi:10.1139/v71-515

17. H. Sun, S. G. DiMagno, Anhydrous tetrabutylammonium fluoride. *J. Am. Chem. Soc.* **127**, 2050–2051 (2005). doi:10.1021/ja0440497 Medline

18. K. O. Christe, W. W. Wilson, R. D. Wilson, R. Bau, J. A. Feng, Syntheses, properties, and structures of anhydrous tetramethylammonium fluoride and its 1:1 adduct with trans-3-amino-2-butenenitrile. *J. Am. Chem. Soc.* **112**, 7619–7625 (1990). doi:10.1021/ja00177a025

19. A. R. Mahjoub, X. Zhang, K. Seppelt, Reactions of the “naked” fluoride ion: Syntheses and structures of SeF_6^{2-} and BrF_6^-. *Chem. Eur. J.* **1**, 261–265 (1995). doi:10.1002/chem.19950010410

20. See supplementary materials.

21. M. L. Gordin, F. Dai, S. Chen, T. Xu, J. Song, D. Tang, N. Azimi, Z. Zhang, D. Wang, Bis(2,2,2-trifluoroethyl) ether as an electrolyte co-solvent for mitigating self-discharge in lithium-sulfur batteries. *ACS Appl. Mater. Interfaces* **6**, 8006–8010 (2014). doi:10.1021/am501665s Medline

22. R. K. Sharma, J. L. Fry, Instability of anhydrous tetra-n-alkylammonium fluorides. *J. Org. Chem.* **48**, 2112–2114 (1983). doi:10.1021/jo00160a041

23. J.-H. Shin, W. A. Henderson, S. Passerini, Ionic liquids to the rescue? Overcoming the ionic conductivity limitations of polymer electrolytes. *Electrochem. Commun.* **5**, 1016–1020 (2003). doi:10.1016/j.elecom.2003.09.017

24. D. T. Thieu, M. H. Fawey, H. Bhatia, T. Diemant, V. S. K. Chakravadhanula, R. J. Behm, C. Kübel, M. Fichtner, CuF_2 as reversible cathode for fluoride ion batteries. *Adv. Funct. Mater.* **27**, 1701051 (2017). doi:10.1002/adfm.201701051

25. P. Verma, P. Maire, P. Novák, A review of the features and analyses of the solid electrolyte interphase in Li-ion batteries. *Electrochim. Acta* **55**, 6332–6341 (2010). doi:10.1016/j.electacta.2010.05.072

26. R. Ghosh Chaudhuri, S. Paria, Core/shell nanoparticles: Classes, properties, synthesis mechanisms, characterization, and applications. *Chem. Rev.* **112**, 2373–2433 (2012). doi:10.1021/cr100449n Medline

27. G. G. Amatucci, N. Pereira, Fluoride based electrode materials for advanced energy storage devices. *J. Fluor. Chem.* **128**, 243–262 (2007). doi:10.1016/j.jfluchem.2006.11.016

28. A. B. Pangborn, M. A. Giardello, R. H. Grubbs, R. K. Rosen, F. J. Timmers, Safe and convenient procedure for solvent purification. *Organometallics* **15**, 1518–1520 (1996). doi:10.1021/om9503712

29. J. E. Anderson, D. Casarini, A. I. Ijeh, L. Lunazzi, Preference for eclipsed conformations in acyclic neopentyldialkylamines and the stereodynamical consequences: An NMR and molecular mechanics investigation. *J. Am. Chem. Soc.* **119**, 8050–8057 (1997). doi:10.1021/ja9710363

30. J. E. Anderson, D. A. Tocher, D. Casarini, L. Lunazzi, Conformational studies by dynamic NMR. 39. Clefts in simple acyclic organic molecules. Corrected stereodynamics of N-tert-alkylbenzylamines studied by dynamic NMR spectroscopy, X-ray diffraction, and molecular mechanics calculations. *J. Org. Chem.* **56**, 1731–1739 (1991). doi:10.1021/jo00005a016

31. E. J. Olson, P. Buhlmann, Unbiased assessment of electrochemical windows: Minimizing mass transfer effects on the evaluation of anodic and cathodic limits. *J. Electrochem. Soc.* **160**, A320–A323 (2013). doi:10.1149/2.068302jes

32. S. Plimpton, Fast parallel algorithms for short-range molecular dynamics. *J. Comput. Phys.* **117**, 1–19 (1995). doi:10.1006/jcph.1995.1039

33. W. M. Brown, A. Kohlmeyer, S. J. Plimpton, A. N. Tharrington, Implementing molecular dynamics on hybrid high performance computers - Particle-particle particle-mesh. *Comput. Phys. Commun.* **183**, 449–459 (2012). doi:10.1016/j.cpc.2011.10.012

34. G. J. Martyna, D. J. Tobias, M. L. Klein, Constant pressure molecular dynamics algorithms. *J. Chem. Phys.* **101**, 4177–4189 (1994). doi:10.1063/1.467468

35. F. Neese, Software update: The ORCA program system, version 4.0. *Wiley Interdiscip. Rev. Comput. Mol. Sci.* **2**, 73–78 (2011). doi:10.1002/wcms.81

36. B. M. Savoie, M. A. Webb, T. F. Miller 3rd, Enhancing cation diffusion and suppressing anion diffusion via Lewis-acidic polymer electrolytes. *J. Phys. Chem. Lett.* **8**, 641–646 (2017). doi:10.1021/acs.jpclett.6b02662 Medline

37. W. L. Jorgensen, D. S. Maxwell, J. Tirado-Rives, Development and testing of the OPLS all-atom force field on conformational energetics and properties of organic liquids. *J. Am. Chem. Soc.* **118**, 11225–11236 (1996). doi:10.1021/ja9621760

38. A. K. Rappé, C. J. Casewit, K. S. Colwell, W. A. Goddard, W. M. Skiff, UFF, a full periodic table force field for molecular mechanics and molecular dynamics simulations. *J. Am. Chem. Soc.* **114**, 10024–10035 (1992). doi:10.1021/ja00051a040

39. C. M. Breneman, K. B. Wiberg, Determining atom-centered monopoles from molecular electrostatic potentials. The need for high sampling density in formamide conformational analysis. *J. Comput. Chem.* **11**, 361–373 (1990). doi:10.1002/jcc.540110311

40. F. G. Bordwell, G. E. Drucker, H. E. Fried, Acidities of carbon and nitrogen acids: The aromaticity of the cyclopentadienyl anion. *J. Org. Chem.* **46**, 632–635 (1981). doi:10.1021/jo00316a032

41. E. M. Arnett, S. G. Maroldo, S. L. Schilling, J. A. Harrelson, Ion pairing and reactivity of enolate anions. 5. Thermodynamics of ionization of p- di- and tricarbonyl compounds in dimethyl sulfoxide solution and ion pairing of their alkali salts. *J. Am. Chem. Soc.* **106**, 6759–6767 (1984). doi:10.1021/ja00334a049

42. F. G. Bordwell, Equilibrium acidities in dimethyl sulfoxide solution. *Acc. Chem. Res.* **21**, 456–463 (1988). doi:10.1021/ar00156a004

43. F. G. Bordwell, M. Van Der Puy, N. R. Vanier, Carbon acids. 8. The trimethylammonio group as a model for assessing the polar effects of electron-withdrawing groups. *J. Org. Chem.* **41**, 1883–1885 (1976). doi:10.1021/jo00872a049

44. K. O. Christe, W. W. Wilson, Reaction of the fluoride anion with acetonitrile, chloroform and methylene chloride. *J. Fluor. Chem.* **47**, 117–120 (1990). doi:10.1016/S0022-1139(00)80453-4

45. M. Videa, W. Xu, B. Geil, R. Marzke, C. A. Angell, High Li^+ self-diffusivity and transport number in novel electrolyte solutions. *J. Electrochem. Soc.* **145**, A1352–A1356 (2001). doi:10.1149/1.1415030

46. K. Hayamizu, E. Akiba, T. Bando, Y. Aihara, ^1H, ^7Li, and ^{19}F nuclear magnetic resonance and ionic conductivity studies for liquid electrolytes composed of glymes and polyetheneglycol dimethyl ethers. *J. Chem. Phys.* **117**, 5929–5939 (2002). doi:10.1063/1.1501279

47. J. H. Kennedy, J. C. Hunter, Thin-film galvanic cell $Pb/PbF_2/PbF_2$, CuF_2/Cu. *J. Electrochem. Soc.* **123**, 10–14 (1976). doi:10.1149/1.2132740

48. J. Schoonman, A solid-state galvanic cell with fluoride-conducting electrolytes. *J. Electrochem. Soc.* **123**, 1772 (1976). doi:10.1149/1.2132694

49. J. Schoonman, K. E. D. Wapenaar, G. Oversluizen, G. J. Dirksen, Fluoride-conducting solid electrolytes in galvanic cells. *J. Electrochem. Soc.* **126**, 709–713 (1979). doi:10.1149/1.2129125

50. G. W. Mellors, U.S. Patent 4,218,527 (1980).

51. G. W. Mellors, U.S. Patent 4,216,279 (1980).

52. L. L. Garza Tovar, P. A. Connor, F. Belliard, L. M. Torres-Martinez, J. T. S. Irvine, Investigation of lead tin fluorides as possible negative electrodes for Li-ion batteries. *J. Power Sources* **97–98**, 258–261 (2001). doi:10.1016/S0378-7753(01)00533-X

53. F. Fujisaki, K. Mori, M. Yonemura, Y. Ishikawa, T. Kamiyama, T. Otomo, E. Matsubara, T. Fukunaga, Mechanical synthesis and structural properties of the fast fluoride-ion conductor $PbSn_4$. *J. Solid State Chem.* **253**, 287–293 (2017). doi:10.1016/j.jssc.2017.06.007